Structure and rheology of organoclay suspensions

H. E. King, Jr., Scott T. Milner, Min Y. Lin,* John P. Singh,† and T. G. Mason‡

ExxonMobil Research and Engineering Company Corporate Strategic Research, Annandale, New Jersey 08801, USA
(Received 11 June 2006; published 21 February 2007)

We have characterized a montmorillonite-based organoclay dispersed in three different nonaqueous solvents using a combination of x-ray scattering, small-angle neutron scattering (SANS), and ultrasmall angle neutron scattering (USANS), together with rheological measurements. Consistent with these measurements, we present a structural model for the incompletely dispersed clay as consisting of randomly oriented tactoids made of partially overlapping clay sheets, with transverse dimensions of several microns. Intersheet correlation peaks are visible in x-ray scattering, and quantitatively fit by our model structure factor. SANS and USANS together show a power law of about −3 over a wide range of wave numbers below the intersheet correlation peak. Our model relates this power law to a power law distribution of the number of locally overlapping layers in a tactoid. The rheology data show that both storage and loss moduli, as well as yield stress, scale with a power law in volume fraction of about three. Equating the gel onset composition with the overlap of randomly oriented tactoids and taking into account the large transverse dimensions of the tactoids, we predict the gel point to be at or below 0.006 volume fraction organoclay. This is consistent with the rheology data.

I. INTRODUCTION

A. Applications of organoclays

Organoclays are widely used to control the rheology of hydrocarbon fluids. They are used as flow modifiers in a surprisingly wide range of applications. Some examples include: oil-field drilling fluids, paints, and lubricating greases [1].

A common characteristic of these applications is the need for a moderate steady-shear viscosity, together with the formation of a strong gel upon cessation of shear. A significant advantage of clays is that these rheological properties are produced economically, i.e., at low volume fractions. In addition, organoclays exhibit good thermal stability (making their use possible where polymer thickening agents would fail). The gels they form are also resistant to gel-breaking effects from other chemicals.

Considerable effort has been expended developing correlations between structure and rheological behavior. Dispersion is recognized as key and is often measured by changes in the interlamellar x-ray scattering peak. There are further suggestions that intersheet binding is important to the rheology. Hydrogen-bonded linkages, induced by added water, are implicated [2].

Recently organoclays have attracted great interest in the emerging field of nanocomposites [3]. Such as the rheological applications, dispersion of the organoclay is seen as essential to the property enhancements for these polymer-based composites. Experiment and theory show that this can be economically attractive because performance enhancements, such as enhanced modulus or improved diffusion barrier properties, are attained at low filler contents.

In developing clay-based nanocomposites or other applications of clay dispersions, it is evidently essential to be able to characterize the state of dispersion of the clay. Measurements of the enhancement of the properties of interest, whether mechanical, rheological, or diffusional, are themselves only indirect indicators of dispersion and therefore not well suited to diagnosis of poorly dispersed clay.

Instead, techniques for studying the arrangement of clay platelets in space have been pursued; namely, electron microscopy and scattering techniques, including light, x-ray, and neutron scattering. X-ray and neutron scattering in particular cover a range of length scales useful for studying the internal structure and overall dimensions of clay platelets and aggregates.

To make best use of these scattering techniques in characterizing clay dispersion, we need calculations of the scattering from physically reasonable models of the structure of clay aggregates, the parameters of which can be determined from comparison to x-ray and neutron data. In this paper we present x-ray, small-angle neutron scattering (SANS) and ultrasmall angle neutron scattering (USANS) from organoclay dispersions in low molecular weight nonaqueous solvents, together with a model for the geometry of and scattering from incompletely dispersed clay aggregates. Our model, with physically reasonable values of four well-defined model parameters, accounts well for the scattering data, and allows us with good confidence to infer the structure of clay tactoids in our samples.

B. Organoclay composition

Clay is a material composed of nanoscale crystalline oxide sheets that can be dispersed into many liquids. This wide compatibility results from changes in the surface chemistry of the oxide sheets. Through changes in surface chemistry,

*Present address: P.O. Box 3862, Gaithersburg, MD 20885. Previously at National Institute for Standards and Technology.

†Present address: Benjamin Levich Institute, The City College of New York, 160 Convent Ave., New York, NY 10031.

‡Present address: Department of Chemistry and Biochemistry, University of California at Los Angeles, 607 Charles E. Young Dr. East, Box 951569, Los Angeles, CA 90095.

the clay is transformed from hydrophilic to hydrophobic.

Natural clays are hydrophilic. The 2:1 structured clays discussed here are composed of crystalline metal-oxide sheets containing a three-layer sandwich, approximately 10 Å thick, with two layers of tetrahedrally-coordinated metal ions surrounding a layer of octahedrally coordinated ones [4]. Although the majority of the tetrahedral sites are occupied by silicon, other cations such as aluminum can substitute, causing the overall charge of the oxide layer to vary from 0 to −2 per sheet.

Inorganic clays compensate for the charge imbalance through interlamellar cations such as sodium. Alteration to a hydrophobic organoclay, the material of primary interest here, is achieved by coating each oxide sheet with a surfactant layer. These surfactant coats self-assemble [5] onto the sheets due to electrostatic attraction between the surfactant headgroup and the surface charge of the oxide sheet.

Producing these organoclays is accomplished by ion exchange of the interlamellar cations for cationic surfactants, such as dimethyldioctadecy-ammonium. This ion exchange proceeds readily for smectite-family clays, with Na-montmorillonite, $Na_{0.7}$ $(Al_{3.3}Mg_{0.7})Si_8$ O_{20} OH_4 being a prototypic example. Once coated, these sheets then further congregate into multisheet stacks.

The surfactant layers themselves form two-dimensional (2D) structures typical of many other surfactant systems such as Langmuir-Blodgett monolayers. Similar to those systems, various structures arise as the surface concentration of surfactant changes [6].

For organoclays an unusual overstuffed condition can occur. In the Na-montmorillonite example, the oxide surface charge is $1e$ per 130 Å^2. Thus the surface coverage for stoichiometric singly-charged surfactants is rather low compared to aliphatic packing densities, which are about 20 Å^2 per chain in the rotator state [7]. As a consequence, "extra" surfactant beyond that required for charge neutrality can be incorporated into the intersheet galleries. These charge-neutral surfactants (balanced by assimilation of anions along with the surfactants) are incorporated due to van der Waals interactions between the aliphatic chains. For a typical overstuffed organoclay the organic content can be as large as 1.2 mole surfactant per inorganic formula unit. They cause the interlamellar spacing to increase and give surfactant chain densities that approach liquidlike packing. However, they are not electrostatically bound, and as we will discuss below, these extra surfactants can be liberated upon immersion in solvent.

The further assembly of individual organoclay sheets into multisheet stacks is a key feature, and their structure has been a focus of many investigations. For example, structural models for the surfactant layers [6,8] have come largely from examination of the interlamellar spacing response to various modifications of the surfactants. These stacks form spontaneously during processing.

Because dispersion of the organoclay into various media is important to most technical applications, studies of their chemical and mechanical disaggregation are a recurrent theme in the organoclay literature. A survey of this literature shows a substantial number of studies that correlate the change in the interlamellar x-ray scattering peak with this disaggregation. Electron microscopy is also often employed. The term "tactoid" has been coined to describe those stacks having a few sheets.

Only qualitative agreement between the tactoid sizes from such x-ray scattering and those from electron microscopy has been found in previous work [9]. This is likely due to the high degree of disorder in the multisheet stack, which would lead to underestimates of tactoid size from the x-ray scattering. To describe the aggregates in such a dispersion requires a model that captures the structure over a wide size range. We will demonstrate that a successful scattering model can be constructed that spans a range of several orders of magnitude in length scales.

C. Inorganic clay structure and rheology

As a guide to expectations for the much less extensively studied organoclays, it is instructive to briefly review the extensive structure and rheology studies of inorganic clay dispersions. Any such discussion must first narrow the focus to those clays that can be dispersed. Those are the "swellable" or smectite family clays that have electrostatic charges of about 0.7e per formula unit. In the recent literature, nearly all such studies use the synthetic clay Laponite, $Na_{0.7}$ $Mg_{5.5}$ $Li_{0.4}$ Si_8 O_{20} OH_4. It is prepared in the form of disks with a thickness consisting of one sheet, ∼10 Å thick, and having a diameter of about 300 Å.

Although the Laponite aspect ratio (about 30) is significantly smaller than that for montmorillonite (about 150), the uniform size of the synthetic clay makes it attractive for many studies. For both materials, immersion in low-ionic strength water at low clay concentrations renders the clay fully dispersed into single sheets [10–12]. Shang and Rice [13] have derived a model for these montmorillonite sheets showing that they consist of a central oxide core (9.2 Å thick) surrounded by symmetrical sheets of bound water. Their scattering model demonstrates that small-angle x-ray scattering (SAXS) data, when analyzed in the Guinier approximation, must include these bound water layers to attain a reasonable size estimate. High ionic strength causes the sheets to flocculate, a well-known phenomenon that occurs for example during mixing of fresh and seawater in natural marine estuaries. The free energy that drives this behavior is well described by the Derjaguin-Landau-Verwey-Overbeek (DLVO) theory, which includes electrostatic and van der Waals interactions [14].

If low ionic strength is maintained, increasing clay content also induces a change in structure accompanied by a rheological transition to a gel. There has been considerable discussion concerning the resulting structure. Both the nearest-neighbor platelet arrangement and the longer-range correlations are disputed. For near-neighbors, the relative dominance of the edge-to-face "house of cards" structure versus that of the parallel plate "tactoid" stacked structure is disputed [12,15–17].

Saunders *et al.* [17] suggests that pH and ionic strength cause a change in the relative importance of the two and this is a source of the disagreements. Similarly, there is no consensus on the longer-range structure. The scattering intensity

for $q < 10^{-2}$ Å^{-1}, about where the near-neighbor correlation peak occurs, exhibits a power law dependence, $\sim q^x$, where $-3 \leq x < 0$.

Pignon et al. [16] summarize typical observations for the Laponite suspensions. Ramsey et al. [10,18] summarize this behavior for montmorillonite. For Laponite, a $x \approx -3$ region is found for a broad range of q values of about $10^{-4} < q < 10^{-2}$. Then at the very lowest q values ($q < 3 \times 10^{-5}$ Å^{-1}) $x = 0$ is observed. In the intervening q range, two power law dependences are observed depending upon clay volume fraction: $x \approx -1$ for $0.0035 \leq \phi \leq 0.0048$ volume fraction and $x \approx -1.8$ for $0.0060 \leq \phi \leq 0.02$ volume fraction. For montmorillonite, a power law of $x = -2$ is observed at low concentrations, (~ 1 wt. %), evolving to SANS that exhibits an interparticle correlation peak with increasing clay content (~ 5 wt. %). At higher concentrations (~ 12 wt. %) a power law of $x = -3$ develops.

Examination of a wide range of scattering literature on clay dispersions shows that the $x \approx -3$ regime is a common feature. Such a power law is not associated with any of the well-defined structures one might expect for mesoscale structured materials, leading various authors to propose aggregate structures that might give this power-law behavior.

One proposal is that the sample consists of solvent poor and rich regions, or equivalently dense aggregates and surrounding solvent. If either the aggregates or the solvent rich regions are assumed spherical and polydisperse in size [11], the resulting scattering can exhibit $x = -3$. As shown in Appendix B, the power law in the structure factor for a polydisperse collection of spheres is $q^{-(7-k)}$, where the probability for a sphere to have radius r is assumed to be a power law r^{-k}. (This result holds for $3 < k < 7$, see Appendix B.)

Thus for a particular power-law distribution of spherical aggregates or voids [$P(r) \sim r^{-4}$], a structure factor scaling as q^{-3} is obtained. However, there is no direct evidence for such a distribution of spherical aggregates being present in incompletely dispersed clay suspensions.

A second suggestion [16] is that the aggregates in a clay suspension are surface fractal objects, with a surface fractal dimension appropriately chosen so that a modified Porod scattering law of q^{-3} results. No physical argument or independent evidence for such a structure has been given.

We shall show in Sec. II F below (see also Appendixes A and B) that within a model of tactoids with a power law distribution in the number of overlapping sheets, a power law in the corresponding structure factor may be likewise obtained.

As already indicated, a rheological transition to a gel is observed with increasing clay content. Mourchid et al. [15,19] provide a good description of the observations. As the clay content is increased they observe a transition from a suspension with (1) no yield stress and (2) $G'(\omega)$ lower than $G''(\omega)$ to a gel that exhibits a yield stress and an increasing $G'(\omega)$ with clay content.

This gel transition is sensitive to ionic strength. For example the onset increases from $\phi_0 = 0.0012$ to 0.0074 volume fraction as the ionic strength is lowered from 10^{-2} to 10^{-4} M. Independent of ionic strength, Mourchid et al. find that all such gels exhibit a power law scaling of the form $G' \sim (\phi - \phi_0)^{2.3}$. They suggest that this implies a gel structure that is independent of ionic strength. They also note another transition at higher clay content where birefringence is observed. This transition is also ionic strength dependent but, unlike the first gel transition, it moves to higher clay content at higher ionic strength.

Pignon et al. also examined the rheology of the Laponite system and combined this with scattering measurements of its structure. There the sol-gel transition occurs at slightly lower clay content than Mourchid's results would suggest. More significantly, Pignon et al. report that upon increasing the clay content there is a rheological transition accompanied by a change in the gel structure. Near to the gel transition, $0.0035 \leq \phi \leq 0.0048$ volume fraction, the yield stress τ follows a power law scaling of the form $\tau \sim \phi^2$. The scattering intensity in this same range exhibits a $x = -1$ power law.

Further into the gel state, $0.0060 \leq \phi \leq 0.02$ volume fraction, the yield stress follows a power law scaling of $\tau \sim \phi^3$. There is a corresponding change in scattering to $x = -1.8$. Pignon et al. show that the fractal dimensions extracted from the scattering can be related to the power laws observed for the yield stress [20]. These observations seem to differ from those of Mourchid et al., which show a universal power law scaling for G' throughout the entire composition range. Due to differences in compositions and no mention of birefringence by Pignon et al., it is speculative to equate this structural change with the onset of birefringence seen by Mourchid et al.

D. Organoclay structure and rheology

There is a rich literature on the behavior of organoclays. We have already mentioned the many studies that examine the interlayer surfactant arrangements (studies that examine the influence of surfactant type and concentration ranges). If we take that variation and now extend those studies to include the influences of various hydrocarbon fluids, including binary and ternary mixtures as are used commercially, an even larger range of literature emerges.

Parts of this literature are summarized in useful reviews [1,21]. Because of the specificity of these studies to the technology of interest, it is challenging to generalize the organoclay behavior. We focus on the properties of interest here and direct the reader to the general references for a more complete picture.

Essentially all applications require that the organoclay be dispersed into a predominately hydrocarbon medium. Factors affecting the ease of dispersion include the type and concentration of surfactant, the polarity of the solvent, the presence of water, and the intensity and duration of shearing. Unlike inorganic clays, full dispersion of the organoclay into single sheets is rarely achieved. This is established by various means, such as x-ray diffraction and electron microscopy. However, a qualitative measure suggesting that dispersion is typically incomplete is that organoclay suspensions are nearly always turbid [22].

The gel transition is of critical importance to most applications. Changing the solvent properties is the preferred means to induce the gel state. Cody et al. [2,23] depict the

gel formation in that case as being a two step process. First a dispersed organoclay suspension is created, and then the dispersed organoclay fragments are bound together via intersheet bridging through hydrogen bonding, facilitated by additives or water molecules. There is an extensive literature examining gel strength as a function of blending of polar and nonpolar solvents. The insight into the underlying physics governing this behavior is obscured by the use of industrial measures of gel strength (such as penetrator insertion depth or flow time through a funnel) and the very high concentration of clay ($\sim$20 wt. %), well above any percolation threshold.

Although no direct connection to rheological behavior is established, Ho *et al.* [22,24] examined the role of the solubility parameter on organoclay dispersion. They conclude that the dispersion-force component of the multicomponent solubility parameter is most important for dispersion. The polar and hydrogen-bonding components seem to control tactoid formation or precipitation. Needed are systematic studies of the effect of clay concentration on the finite-strain rheological response of organoclay-solvent systems, which is an objective of the current study.

We have already established that inorganic clay suspensions pose an as-yet unresolved structural puzzle. Organoclays are less well studied, but we expect similar features. Here, the nearest-neighbor orientation seemingly favors tactoids, as evidenced by the prevalence of incomplete dispersion from multilayer stacks into single sheets. On a longer length scale, examination of recent SAXS and SANS studies [22,25] suggests that, such as the inorganic clays, the scattered intensity for these systems often exhibits a power law of the form $I \sim q^{-x}$, where $x \approx 3$. By combining SANS and USANS, Yoonessi *et al.* [25] show that this power law behavior persists over a very wide q range.

We discussed above that the inorganic clay structure associated with this power law behavior is ambiguous. One caution to be used in comparing the two systems is a considerably larger aspect ratio for the organoclay than for Laponite. This, for example, could force the scattering for large-scale structures outside the window for x-ray or neutron scattering. This might explain the absence of rollover to shallower slopes as is observed for Laponite by Pignon *et al.* [16]. We therefore focus in our remaining discussion on the $x \approx 3$ power law region for the organoclays.

Ho *et al.* [22] were among the first to carefully examine the structure of organoclay suspensions using SANS. Recognizing that the commercially available organoclays contain excess surfactant and are polydisperse in size, they used Soxhelet extraction combined with sedimentation to purify the samples prior to dispersing them into various solvents. According to their Table I, the purified samples can sometimes give transparent gels. However, these same gels exhibit SAXS profiles showing that tactoids are still present. Furthermore, comparison of SAXS profiles and SANS data shows that there is no qualitative difference between the extracted and unextracted samples. This is consistent with subsequent measurements [26] suggesting that the surfactant molecules are liberated by immersion in solvent. We quantify that result below.

SANS data for the four solvents (chloroform, benzene, toluene, and *p*-xylene) that are reported to form gels in Table I of Ho *et al.*, all exhibit power law slopes steeper than -2, the theoretical value for dispersed plates. Chloroform displays the smallest deviation (about -2.2), and Ho *et al.* demonstrate that a scattering model consisting of a single, surfactant-coated inorganic disk can describe this data. This model cannot describe the other three materials. For these three samples, a common power law slope of $x \sim -2.36$ is reported for the low-q region. Further, Ho *et al.* report that even for very dilute concentrations (0.1 wt. % $\sim$ 0.0005 volume fraction) their single-plate model cannot describe the scattering.

Acknowledging the need to include multisheet stacking in their scattering model, Ho *et al.* convolve the Kratky-Porod one-dimensional (1D) paracrystalline correlation function with the single-plate scattering form factor. The use of this function for multilayer stacks of disklike objects is well known [27]. In its finite stack size formulation, this introduces three parameters, the average interlayer spacing Δ, the standard deviation from this average value ξ, and the number of layers per stack (N). Figures demonstrating how variations in these parameters alter the function are shown in recent publications [9,27].

Here, we focus on the predicted intensity increase approaching $q=0$. Accompanying this rise, the Kratky-Porod function produces a series of oscillations with decreasing q. These interference features, due to a tactoid of a definite and finite thickness (see for example Fig. 5 in Hanley *et al.* [26]), have a period equal to 2π/thickness. Such oscillations are not observed in the scattering data.

Ho *et al.* [22] claim that these oscillations of the Kratky-Porod function are damped in the calculation of the full structure factor by the averaging over angle between the normal to the stacking direction and the scattering vector. However, as we demonstrate in Sec. II F and Appendix A, the integral over tactoid orientations has little effect in damping these oscillations. This is because the scattering from tactoids of large aspect ratio is dominantly into a small angular region defined by the angle between the sheet normal and the wave vector being less than order $1/(qR)$. As a result, to a very good approximation, the resonance structure of the Kratky-Porod function survives in the final structure factor.

In summary, the Kratky-Porod treatment, in which the sheets are described as infinite flat parallel planes with a nearly regular spacing and a finite number of layers, is a physically sensible starting point to describe the structure of partially exfoliated clay. But if we are to apply this function, we will require a mechanism by which the oscillations in the structure factor are to be damped.

Below, we present a formulation where we average over a distribution of the number of layers per stack. We expect that polydispersity in the number of layers per stack will wash out oscillations corresponding to interference effects of a stack of a definite thickness. This approach indeed eliminates the spurious oscillations, and results in excellent fits that describe the data over the entire q range. Furthermore, the fit parameters are consistent with other estimates of tactoid size.

TABLE I. Materials used in this study.

Material	Composition	Density, g/cc	Neutron SLD, cm^2	X-ray SLD, e cm^{-3}
dimethyldioctadecy-ammonium (DTDM)	$[CH_3(CH_2)_{17}]_2N(CH_3)_2$	0.75[a]	-3.051×10^9	2.582×10^{23}
Na-Montmorillonite-layer	$Na_{0.7}(Al_{3.3}Mg_{0.7})Si_8O_{20}OH_4$	2.851[b]	4.093×10^{10}	8.575×10^{23}
Cloisite 6A	$DTDM_n(Al_{3.3}Mg_{0.7})Si_8O_{20}OH_4$	1.240	see text	see text
p-xylene-d10	$C_6H_4(CH_3)_2$	0.948	5.89×10^{10}	2.850×10^{23}
tetrahydrofuran-d8 (TDF)	C_4D_8O	0.985	6.346×10^{10}	2.961×10^{23}
chloroform- d1 (CDCl$_3$)	C D Cl$_3$	1.505	3.166×10^{10}	—
DTDM/p-xylene layer at contrast match	ϕDTDM=0.491 ϕp-xylene (H to D93:7)=0.509	—	4.254×10^9	—
DTDM/p-xylene-d10 layer	ϕp-xylene-d10=0.509	—	2.848×10^{10}	2.699×10^{23}
DTDM/TDF layer	ϕTDF=0.509	—	3.080×10^{10}	2.775×10^{23}
DTDM/CDCl$_3$ layer	ϕCDCl$_3$=0.509	—	1.462×10^{10}	—

[a]Density calculated from molecular dimensions [28] of area=47 Å^2 and length=26 Å.
[b]Density calculated from layer volume per formula unit of $5.18 \times 9.0 \times 9.2$ Å derived from unit cell dimensions [4].

II. SANS, SAXS RESULTS

A. Materials

For our studies, we used a commercially prepared organoclay, Cloisite 6A from Southern Clay Products.[1] This Montmorillonite-based material is a dry, easy-flowing powder that consists of 46.4 wt. % organic content as measured by differential thermogravometric analysis (DTA). The cationic surfactant is $[CH_3(CH2)_n]_2N(CH_3)_2$ with components n=17, 15, and 13 mixed by weight in the ratio 65:30:5. We approximate this mixture as dimethyldioctadecy-ammonium (n=17) that we hereafter designate as DTDM.

From the measured organic content we calculate a molar fraction DTDM per inorganic formula unit >1. Using the densities in Table I, an overall density of 1.240 g/cc is obtained. Southern Clay Products reports that the surfactant content is 1.40 meq/gm; taking the densities from Table I, this indicates an organic content of 44 wt. % or about 1 mole DTDM per formula unit, in reasonable agreement with our values. In a recent study [22] Closite 15A was utilized. For comparison with our results, we note that this material differs only in surfactant content. We measure the organic content of

that clay as 44.2 wt. %; the manufacturer indicates that the surfactant content is 1.25 meq/gm (41.1 wt. %). Water content of the organoclay may account for some of the discrepancy between the quoted organic contents and those calculated from DTA data.

Small angle x-ray scattering (SAXS) measurements on such powders corroborate the relative surfactant content. For 6A and 15A, the respective interlayer spacings are $\Delta \sim 35$ Å and $\Delta \sim 33$ Å. As noted by others [4], these interlayer spacings do not reflect a fully-extended double layer of surfactant molecules between each inorganic sheet. If each surfactant extended to its full length, 26 Å, the surfactant density would be low; therefore chain packing maintains the smaller spacing for these dry powders. Immersion in a good solvent considerably expands the layer.

Three deuterated solvents, all obtained from Aldrich and used as received, were utilized in these studies. Their properties are listed in Table I. An important consideration in selecting these solvents was their ability to disperse the organoclay. It has been suggested that the solubility coefficient is a key measure of this ability [22,24]. The organoclay literature [1] indicates that polar substances have a strong effect.

Following the convention of Wiehe [29] we relate the polar character of the solvent to the magnitude of the δ_c component of his two-dimensional solubility coefficients. Our three solvents have the following solubility coordinates (δ_f, δ_c) [both in units of (MPa)$^{1/2}$]: tetrahydrofuran (16.81, 9.82); chloroform (17.69, 6.16); and p-xylene, (18.04, 0.82).

These three have δ_f components that vary little ($\sim 7\%$) compared to the variation in δ_c ($\sim 1000\%$). As we will show, the resulting tactoid structure varies little across this series.

Samples consisting of Cloisite 6A clay powder and the selected solvent were prepared in ~ 10 cc volumes and mixed using a conventional magnetic stir bar for a period of about 1 day. These fluids were turbid, slightly colored and highly viscous. Examination of the *p*-xylene samples with phase-contrast microscopy revealed that the samples contain a small fraction of birefringent, crystalline fragments with lateral dimensions of 70×150 μm^2. The thickness of these plates is difficult to determine, but it is considerably smaller than the lateral dimensions. These plates apparently form in situ. Their dimensions exceed the particle sizes in the as-received powder, and the plates have exceedingly sharp, straight edges typical of crystal growth. The number of such plates per unit volume increases with clay content. It is likely that these particles contribute to the birefringent regions observed when the bulk solutions are examined between crossed polarizers. Such appearance is typical for the samples containing more than 1 wt. percent Cloisite 6A in *p*-xylene.

B. Scattering experiments

1. SANS and USANS

For neutron scattering, the fluid samples described above were loaded into circular quartz cuvettes having sample thicknesses (~ 0.2 cm) dictated by the attenuation coefficient of that sample. The fluids were loaded through use of a syringe, producing a moderate degree of shear strain. However, no time dependence to the SANS was observed for sampling times that extended over several days.

All neutron scattering experiments were performed at the NIST Center for Neutron Research (NCNR), in Gaithersburg, Maryland. Conventional SANS data were obtained using the NG7 NIST/ExxonMobil 30-m SANS instrument. With two detector-sample distance configurations and a neutron wavelength of 8 Å, a *q* range of 0.0008 to 0.3 Å^{-1} was obtained. Scattered intensities were collected with a 2D detector, and data reduction and normalization followed standard procedures [30]. The resolution is mainly determined by the $\Delta\lambda/\lambda = 0.1$. We calculated the full smearing function using the methods of Barker and Pedersen [31] and found that over most of the *q* range the width of the resolution was less than 10% of the *q* value. This indicates that oscillations of the sort predicted by the Kratky-Porod function for finite tactoid size (with ~ 10 layers) would have been easily resolved if present. The critical fits of the scattering functions described in the present work, power law decay at small *q* values, are little affected by application of the smearing function and it is not included in our fits.

Scattered and transmitted intensities were measured at the same configuration with the sample (I_r, T), without the sample (i.e., only the empty sample cell (I_e, T_e), and with the neutron incident beam blocked at the sample position (I_b). The scattered intensities (in arbitrary units) due only from the sample are then produced through the following relation:

$$I(q) = I_r - I_e - (I_e - I_b)\frac{T}{T_e}. \tag{1}$$

These intensities are then compared with a known secondary standard. Its transmission (T_s) and pathlength (d_s) are known and its intensities (I_s) are measured at the same configuration as our sample to obtain the normalized cross-section per unit volume of the sample in a unit of cm^{-1}

$$\frac{d\Sigma(q)}{d\Omega} = \frac{I(q)d_sT_s}{I_s(0)Td}\frac{d\Sigma_s(0)}{d\Omega}, \tag{2}$$

where $d = 0.2$ cm is the path length of the sample and $d\Sigma_s(0)/d\Omega$ is the known crossection of the standard at $q = 0$.

Ultrasmall angle neutron scattering data were obtained also at NCNR, with the BT5-USANS instrument. The US-ANS instrument is a double crystal diffractometer, using a one-dimensional arm scan to perform angular measurements of the scattering at a wavelength of 2.38 Å [32]. The *q* range is from 0.000 03 to 0.002 Å^{-1}, allowing overlap with the SANS data. Similar background and empty cell measurements were also performed and data reduced in a similar fashion. However, the USANS data are taken with a slit geometry. To compare with the SANS data, taken with a pinhole geometry, the USANS data reduction also includes a de-smearing procedure [33].

2. SAXS

The SAXS data were collected using x-rays produced from an 18 kW Rigaku rotating anode generator. Typical operating conditions were 55 kV and 280 mA. The Cu $K\alpha$ radiation is monochromated and collimated through use of a vertically-focusing graphite monochromator. The wavelength is approximately 1.54 Å. The sample is mounted on a Huber 2-circle goniometer that has vertical and horizontal motorized sample-positioning allowing for precise placement of the sample in the x-ray beam. The diffracted radiation is measured through use of a one-dimensional arm scan. The resolution, typical value FWHM of 0.11 degree measured at $q = 0$, is defined through a combination of the incident and diffracted slit widths.

The samples were held in $1-3$ mm diameter glass capillaries. As described above, samples of about 10 ml were first prepared, and this mixture was then loaded into the glass capillary by use of a syringe. Each capillary tube was sealed to prevent vapor loss during the experiments. To check for sample evolution, observations were made immediately upon loading, after 24 h, then several days later; no changes in the SAXS were observed. The diameter of the capillary for each sample was selected to give a transmission of about 0.3 thus ensuring that uniform scattering was obtained throughout the bulk of the sample. Due to the high attenuation of CHCl$_3$, no observations could be made at this photon energy. Qualitative measurements were made at the Advanced Photon Source using a photon energy of 20 keV.

C. Scattering length

We measured the scattering length density (SLD) of this material by adding a fixed amount of organoclay (1 wt. % or

Analysis Type	Contrast Match (cm^{-2})
q= 0.00134 Å^{-1}	1.1498±0.16x10^{10}
Power Law Fit	1.1138±0.20x10^{10}

Cloisite 6A in p-xylene
Wt. Frac. = 0.011
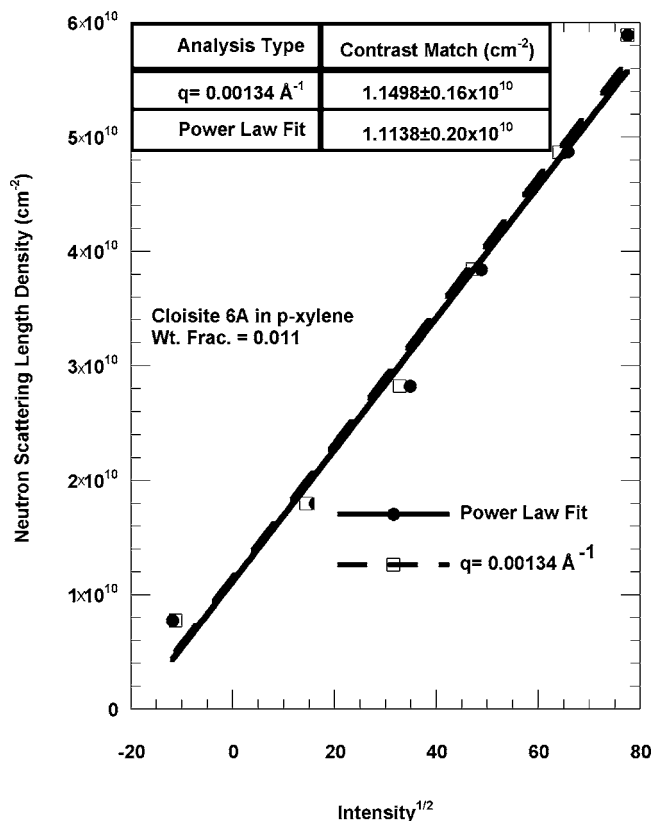
——●—— Power Law Fit

– –□– – q= 0.00134 Å^{-1}

FIG. 1. Two methods to extract the scattering length density for Cloisite 6A. For the power law fits, the intensity was estimated by taking parameters, A, from an equation of the form $Aq^{-2.709}$ fit to each data set. For the second estimate, the intensity at q =0.000 134 Å^{-1} was used for each data set. By averaging these two results we obtain the final SLD : $1.13 \pm 0.18 \times 10^{10}$ cm^{-2}.

0.008 volume fraction) to a set of six liquids representing different p-xylene-h10 to p-xylene$-d$10 ratios. The systematic change in scattered intensity was analyzed in two ways to obtain an overall estimate of the scattering contrast for Cloisite 6A.

We first fit each data set in the low q region, $0.0008 \leq q \leq 0.01$ Å^{-1}, with a power law Aq^X, allowing the prefactors (A) and the exponent values (x) to vary. Exponent values ranging from -2.6176 to -2.8292 were obtained. A common value for the exponent is expected, and indeed, there is no systematic trend in these exponents with composition. Therefore, we refit the data using an average exponent value of -2.709, obtaining the prefactor values for each composition. The square root of these values (recognizing that for p-xylene-h10 the amplitude is negative), when plotted versus the SLD of the fluid, gives a linear correlation (Fig. 1). The calculated contrast-match point for this is $1.114 \pm 0.203 \times 10^{10}$ cm^{-2}. This is one estimate of the SLD of the Cloisite 6A.

An alternative to this fitting procedure is to use the actual intensities measured at a selected q value, $q=0.001\ 34$ Å^{-1}. Those values (Fig. 1), analyzed in a similar fashion to above, give a contrast-match point of $1.150 \pm 0.156 \times 10^{10}$ cm^{-2}.

We average these two estimates to obtain our value for the SLD of Cloisite 6A as $1.13 \pm 0.18 \times 10^{10}$ cm^{-2}.

D. Scattering length density analysis

After we split this result into inorganic and organic contributions, it will emerge that these values are quite informative regarding the clay composition after immersion in solvent.

The required condition to separate the two components is that the observed SLD is the volume-fraction-weighted average of the SLD's of the organic and inorganic components:

$$\phi_{organic} \times n_{organic} + \phi_{inorganic} \times n_{inorganic} = n_{observed}, \quad (3)$$

where n_α is the SLD of component α. Three of the terms on the left of this expression are well known, hence we conclude $n_{organic}=4.254 \times 10^9$ cm^{-2}. This value is positive; therefore, as expected, a fraction of the surfactant layer has been replaced by solvent.

To calculate the solvent-to-DTDM ratio, we equate $n_{organic}$ to the combined solvent and n_{DTDM} *in the organic phase*, $\phi_{DTDM} \times n_{DTDM} + (1 - \phi_{DTDM}) \times n_{solvent}$. Assuming that the trapped solvent has the same H/D ratio (93/7) as the bulk fluid, we obtain $\phi_{DTDM}=0.491$. More than half of the layer is trapped solvent. This value for ϕ_{DTDM} allows us, for the first time, to calculate the inorganic-to-DTDM ratio of an organoclay immersed in a solvent.

Not surprisingly, the value indicates considerable DTDM loss over the starting material. We note that, per clay plate, the dimensions of interlayer spacing (48 Å) shows that the volume fraction organic is $(48-9.2)/48=0.808$. Therefore the volume fraction DTDM per clay sheet is $0.808 \times 0.491 =0.397$. We use the densities for the clay plate and organic layer of 2.851 and 0.75 g/cc respectively to calculate the weight fraction DTDM=0.352. Restated as mole fraction we find that this corresponds to 0.71 moles DTDM per clay sheet, essentially identical to the charge balance composition. We graphically trace the evolution of the organoclay surfactant content in Fig. 2 for both Cloisite 6A and 15A. Both materials, within error, evolve to the same composition, one corresponding to charge-balance composition. Recall that the surfactant was removed from 15A by a solvent extraction method. That both materials achieve a similar composition is significant.

The estimated error on the contrast matching SLD is $\pm 0.18 \times 10^{10}$ cm^{-2}. Using this range, we calculate lower and upper bounds for the weight fraction DTDM of 0.267 to 0.420, corresponding to mole fractions of 0.47 to 0.95. The lower bound is beyond the charge balance composition and is therefore unphysical. The upper bound is a composition slightly below the original surfactant level of 0.464 wt. fraction. Assuming that only hydrogenated p-xylene is trapped, the physically allowed range of calculated compositions is still within this range. Hence, all of our values are consistent with removal of surfactant upon immersion of the organoclay in xylene.

A natural end point for that extraction is the charge-neutral composition of 0.7 mole fraction DTDM. We utilize this composition throughout the remainder of our calculations. This corresponds to setting the volume fraction of DTDM *in the organic layer* to $\phi_{DTDM}=0.491$ and in filling the remaining volume fraction with the solvent, i.e.,
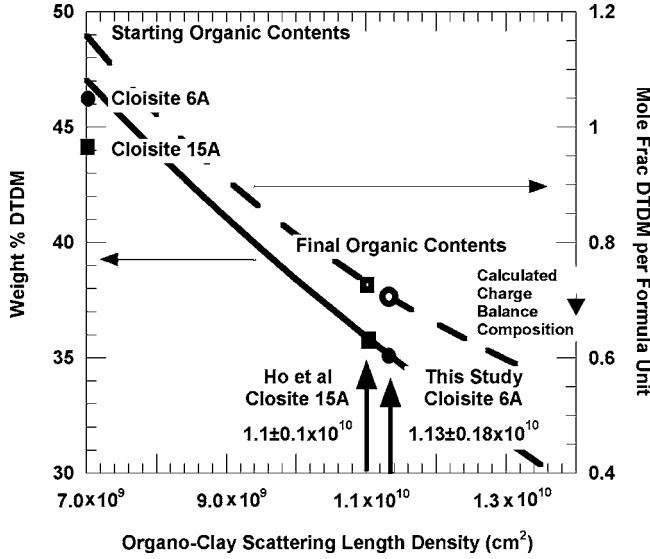
FIG. 2. The relationship between scattering length density (SLD) of the Cloisite-type organoclays and their composition. The as-received organic contents are indicated on the left vertical axis. The experimentally-determined SLD's for Cloisite 15A and 6A [this study] are indicated by the arrows. The wt. percent and mole fraction DTDM corresponding to these SLD's are indicated by, respectively, the solid and open symbols. SLD's for both organoclays are consistent with the expulsion of excess surfactant into the solvent down to that required for charge neutrality, 0.7 mole fraction DTDM.

p-xylene-*d*10, tetrahydrofuran-*d*8 (hereafter TDF) or CDCl$_3$. The resulting SLD values are listed in Table I.

At high organoclay loading a secondary consequence of this DTDM loss is an induced change of $n_{solvent}$ due to the addition of significant hydrogenated material. At 5 wt. % organoclay and below, this effect is small, less than 2% change in SLD. For samples containing above 5 wt. % organoclay, we correct the $n_{solvent}$ for the addition of DTDM. For the 10 and 20 wt. % Cloisite 6A in *p*-xylene-*d*10 this changes the SLD values to 5.794×10^{10} and 5.678×10^{10} cm^{-2}, respectively.

E. Single-sheet scattering

As is evident from our discussion of the organoclay structure, the surfactant-covered oxide plate is the underlying structural unit. Richter *et al.* [27] formulate a rigorous description for the scattering for such a system and we follow their convention in the following discussion.

The core of the organoclay sheet is a 9.2 Å metal oxide of Na-Montmorillonite. Due to the crystalline nature of this material the dimensions and composition of this core are well constrained. We provide the neutron SLD in Table I for a composition consistent with a typical Na-Montmorillonite. This SLD is relatively insensitive to substitution of other elements, such as iron. This core is covered by DTDM layers of surfactant or solvent on both sides.

From the SAXS data we obtain an interlamellar spacing of 48 Å, thus each DTDM layer is 19.4 Å for *p*-xylene-*d*10. As we previously discussed, the DTDM layer expels excess

surfactant and imbibes solvent. We assume the solvent volume fraction determined from the contrast matching experiments, and calculate the SLD here as 2.848×10^{10} cm^{-2}.

To calculate the scattering from such a system of individual plates, well separated in the solvent, we utilize the following formulation following Richter *et al.*

$$C_c(q) = 2h \times 10^{-8} \frac{\sin(qh)}{qh} \exp\left(-\frac{1}{2}q^2\sigma_c^2\right), \quad (4)$$

$$C_b(q) = 2^*(d+h) \times 10^{-8} \frac{\sin(q(d+h))}{q(d+h)} \exp\left(-\frac{1}{2}q^2\sigma_b^2\right) - 2h$$

$$\times 10^{-8} \frac{\sin(qh)}{qh} \exp\left(-\frac{1}{2}q^2\sigma_c^2\right). \quad (5)$$

These terms describe the scattering from the core (C_c) and the surfactant layers (C_b). In this formulation the core thickness is $2h$ and the surfactant layer on each side of this core has thickness d. The square profiles are rounded by the inclusion of Gaussian profiles ($\sigma_b = 4.5$ Å and $\sigma_c = 0.1$ Å). (Note: unlike Richter *et al.*, we are not dealing with diblock polymers; therefore, we can neglect the multiplicative prefactor for C_b describing the fraction of one of the brush components.) We combine these terms along with the SLD contrast factors, $\Delta\rho$, to obtain the overall form factor for an individual plate

$$\tilde{f}(q) = (C_b(q))^2 \Delta\rho_b^2 + 2(C_b(q)C_c(q))\Delta\rho_b\Delta\rho_c + (C_c(q))^2 \Delta\rho_c^2. \quad (6)$$

This is then used to calculate the scattering from an ensemble of plates.

To calculate the total scattering for an ensemble of randomly-oriented single plates we average over the orientation of the sheet normal, following the approach of Richter *et al.* Details may be found in Appendix A. We must also scale the calculation to account for the number of plates per unit volume of solvent. We obtain

$$\frac{d\Sigma}{d\Omega}(q) = \phi_{clay}\frac{v_{core}}{Vc}\tilde{f}(q)(\pi R^2)^2 \times 10^{-32}\frac{D(qR/2)}{qR/2}, \quad (7)$$

where ϕ_{clay} is the volume fraction of organoclay added to the solvent, v_{core} is the volume fraction of inorganic component to organic component in the as-received organoclay, V_C is the volume of the inorganic core in each organoclay sheet. We calculate v_{core} by noting that the weight fraction of organic is 0.464. Using densities of 0.75 g/cc for DTDM and 2.851 g/cc for the inorganic core, $v_{core} = 0.233$. The volume of inorganic for one clay plate is obtained from $V_C = 2h\pi R^2$.

We obtain the single-plate scattering for 0.008 volume fraction Cloisite 6A in *p*-xylene-*d*10 (Fig. 3), where we have added a background of 0.054 cm^{-1}.

F. Scattering from stacks

We model the geometry of dispersed clay as follows. We regard the individual clay sheets as flat disks with large aspect ratio and a given cross-sectional profile. The sheets are
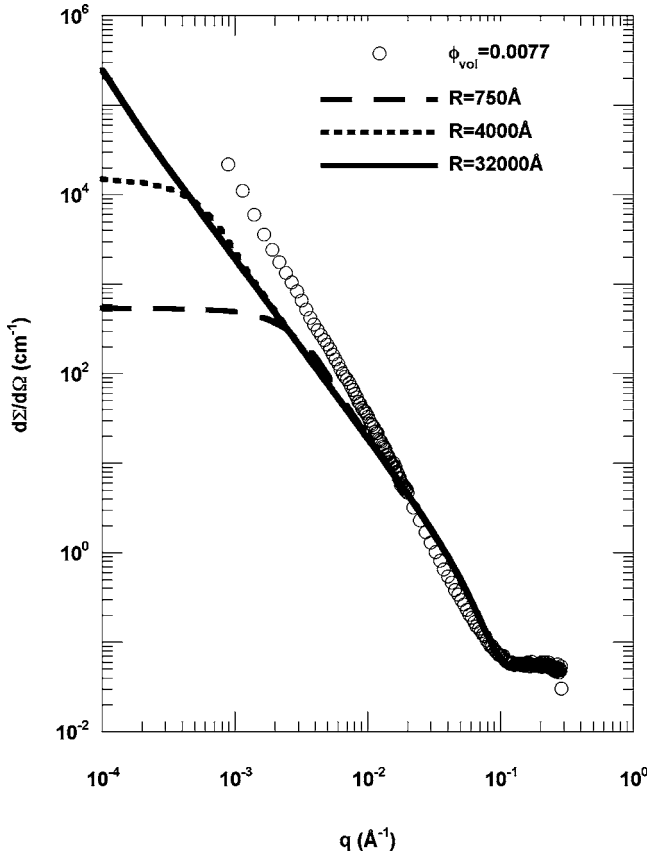
FIG. 3. The SANS data for 0.008 volume fraction Cloisite 6A in p-xylene-d10, circles, are compared with the calculated scattering intensity for powder-averaged, single-plate organoclay sheets. Each sheet consists of a 9.2 Å metal oxide core covered on both faces by a DTDM + solvent layer, 19.4 Å thick. The solid, dotted, and dashed lines demonstrate the effects of decreasing lateral dimension of this disk-shaped object (diameter=2R). Clearly additional structure is present.

assumed to be in stacks with nearly regular spacing, but with some randomness in the distance between adjacent sheets in the stack. The stacks are taken to be randomly oriented, and dilute enough so that we need not consider correlations between the spatial location of one stack and another. Different stacks will have different numbers of sheets; the number of sheets in a stack will have a probability distribution, which we model with a convenient function with two parameters to be determined by fitting to scattering data.

To predict the scattering from dispersed clay, we first compute the structure factor for a stack of n parallel sheets with normal along the z direction. Details are presented in Appendix A. The result is

$$S(q_\perp, q_z) = |\tilde{g}(q_\perp)|^2 |\tilde{f}(q_z)|^2 \Sigma_n(\exp(iq_z\Delta - (1/2)q_z^2\xi^2)). \tag{8}$$

Here $\tilde{g}(q_\perp)$ is the transverse form factor of a disk of radius R; $\tilde{f}(q_z)$ is the cross-sectional form factor; Δ is the average layer spacing; ξ^2 is the variance in separation of adjacent layers in the stack; and $\Sigma_n(X)$ is the Kratky-Porod function

$$\Sigma_n(X) = n + 2\operatorname{Re}\left[\frac{X^{n+1} + nX(1-X) - X}{(1-X)^2}\right]. \tag{9}$$

Then, we average over the orientation of the sheet normal, following the approach of Richter *et al.* [27]. Details may be found in Appendix A. The result is

$$\langle S(q)\rangle_\Omega = |\tilde{f}(q)|^2 \Sigma_n(\exp(iq\Delta - (1/2)q^2\xi^2))\frac{(\pi R^2)^2 D(qR/2)}{(qR/2)} \tag{10}$$

in which $D(u)$ is the Dawson function

$$D(u) = \exp(-u^2)\int_0^u dt \exp(t^2). \tag{11}$$

Now we address the question of polydispersity of the number of sheets n in a stack. We posit a distribution function $P_{k,y}(n)$ of the form

$$P_{k,y}(n) \propto n^{-k}y^n. \tag{12}$$

This form is versatile, in that with it one can represent distributions with varying shapes, ranging from exponential to power-law to nearly Gaussian. It is also well posed, in that it is defined only for positive integer values of n. Finally, it is mathematically convenient, because of the summation identity

$$\sum_{n=1}^\infty n^{-k}y^n = \operatorname{Li}_k(y) \tag{13}$$

in which $\operatorname{Li}_k(y)$ is the polylogarithm function (available in Mathematica, e.g.). Thus, we can define a normalized probability distribution $P_{k,y}(n)$ as

$$P_{k,y}(n) = \frac{n^{-k}y^n}{\operatorname{Li}_k(y)} \tag{14}$$

and evaluate the moments of n as

$$\langle n^j\rangle_P = \frac{\operatorname{Li}_{k-j}(y)}{\operatorname{Li}_k(y)}. \tag{15}$$

Thus, the mean number of layers in the stack $\langle n\rangle$ is $\operatorname{Li}_{k-1}(y)/\operatorname{Li}_k(y)$, and the variance $\langle n^2\rangle - \langle n\rangle^2$ is $[\operatorname{Li}_{k-2}(y)\operatorname{Li}_k(y) - \operatorname{Li}_{k-1}(y)]^2/\operatorname{Li}_k(y)^2$. We can likewise average the Kratky-Porod function $\Sigma_n(X)$ over this distribution, to obtain

$$\Sigma_{k,y}(X) = \frac{\operatorname{Li}_{k-1}(y)}{\operatorname{Li}_k(y)}$$
$$+ 2\operatorname{Re}\left[\frac{X\operatorname{Li}_k(Xy) + X(1-X)\operatorname{Li}_{k-1}(y) - X\operatorname{Li}_k(y)}{\operatorname{Li}_k(y)(1-X)^2}\right]. \tag{16}$$

Replacing the Kratky-Porod function $\Sigma_n(X)$ with its average $\Sigma_{k,y}(X)$ over the distribution $P_{k,y}(n)$ gives our final result for the structure factor

$$\langle S(q)\rangle_{P,\Omega} = |\widetilde{f}(q)|^2 \Sigma_{k,y}(\exp(iq\Delta - (1/2)q^2\xi^2))\frac{(\pi R^2)^2 D(qR/2)}{(qR/2)}. \tag{17}$$

The behavior of this function for small wave number is analyzed in Appendix C. There it is shown that for $y=1$ and $1 < k < 3$ (i.e., power-law distributions of the number of layers per stack), $\langle S(q)\rangle_{P,\Omega}$ goes as q^{k-5} for small wave number (but $qR \gg 1$). Thus, for k around $k=2$, we obtain a power law for the structure factor of about q^{-3}.

Combining the structure factor of Eq. (17) with Eq. (7), we obtain the formulation for total scattering of an ensemble of stacks of clay sheets dispersed in solvent

$$\frac{d\Sigma}{d\Omega}(q) = A\phi\frac{v_{core}}{V_{core}}\widetilde{f}(q)\langle S(q)\rangle_{P,\Omega} + B. \tag{18}$$

Here we introduce an amplitude parameter A to account for deviations in experimental scattering intensity from the theoretical ones. We also add a constant background term B to describe the significant incoherent background.

If we fix the single-sheet parameters [Eq. (6)] required to calculate $P(q)$, Eq. (18) indicates that five additional structural parameters will be needed to describe the scattering: the layer periodicity Δ; the standard deviation of the layer spacing ξ; the parameters k and y characterizing the distribution of the number of layers in a stack; and the plate radius R. In the following sections we examine the predicted values for these parameters from fitting the scattering data.

G. SAXS fits

Comparison of the x-ray and neutron SLD values (Table I) shows that x-ray scattering arises mainly from the contrast between the metal-oxide core and the surrounding organic surfactant tails. This core-contrast form factor accentuates the peak in $S(q)$; whereas, the SANS data exhibit a significant incoherent background, obscuring the intersheet correlation peak. Therefore, the two parameters describing the paracrystalline ordering Δ and ξ are best determined using SAXS data.

The resulting SAXS for *p*-xylene and tetrahydrofuran (hereafter THF) samples are shown in Figs. 3 and 4, where three orders of diffraction maxima from interlamellar peaks are seen. We calculate the x-ray scattering intensity using Eq. (18), with an additional modification to account for slit broadening. Our SAXS data were taken with a slit geometry, requiring this correction, and we use the formulation described in Roe [34] [Eq. (5.170)].

We manually adjusted the value for Δ in increments of 1 Å to reach good agreement with the peak position. We obtain *p*-xylene, $\Delta=48$ Å, and THF, $\Delta=46$ Å. The value for ξ is less sensitive, values between 6 and 1 were explored before selecting $\xi=3$ Å. These values were fixed during refinement of the additional three parameters using the SANS and USANS data. We discuss these fits in the next section.
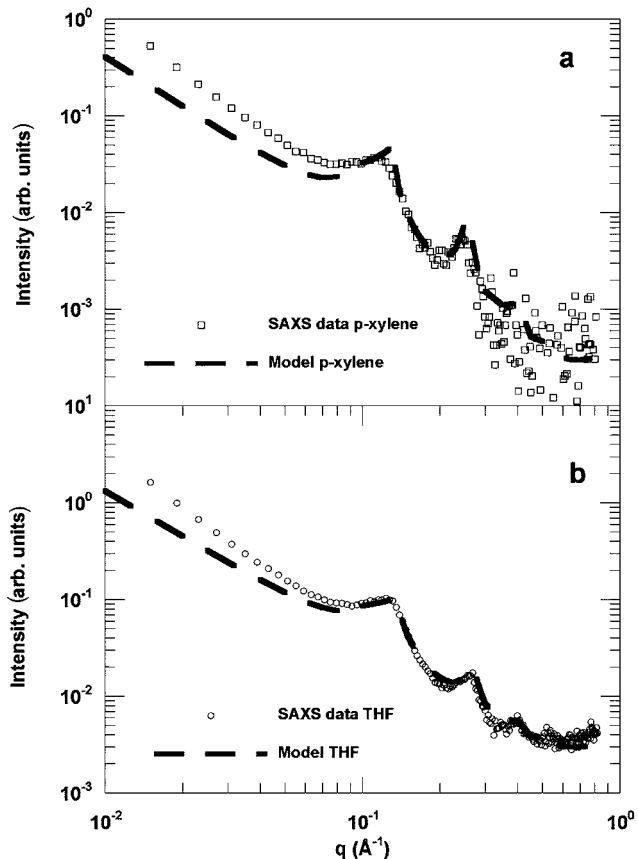

FIG. 4. X-ray scattering data (squares) compared with model (line). Initially these SAXS data are used to fix values of the interlamellar spacing (*p*-xylene, $\Delta=48$ Å, and THF, $\Delta=46$ Å) and the Gaussian deviation about this mean value ($\xi=3$). Subsequently the k parameter of the distribution for the number of layers per stack is optimized using the SANS and USANS data. The models plotted here were calculated from the SANS optimized parameters in Table I, appropriately broadened through use of a finite slit broadening function (see text).

Here we compare the resulting calculated scattering curves with our SAXS data. As these data are not referenced to absolute scattering power, we have freely adjusted A and B. The resulting calculations (Fig. 5) closely reproduce the SAXS peaks. The lower q data exhibit a somewhat different power-law behavior, but this is likely due to our use of a vertically-focusing monochromator. This will introduce slit broadening that cannot be accounted for using the model.

As another comparison with the full model, we fit the first-order maxima with Gaussian peak shapes. The peak widths from those fits, using the Scheerer equation, correspond to average stack heights of 2.1 layers (*p*-xylene) and 2.2 (THF), similar dimensions to those for $\langle N\rangle$ values from the full SANS fit, Table II.

The strong adsorption coefficient for $CDCl_3$ makes x-ray scattering at 8 keV impossible. Therefore, we examined one sample using 20 keV energy photons from synchrotron radiation at the Advanced Photon Source, Argonne. We observed low-intensity SAXS peaks at positions corresponding to $\Delta=48$ Å, but the data are only qualitative.
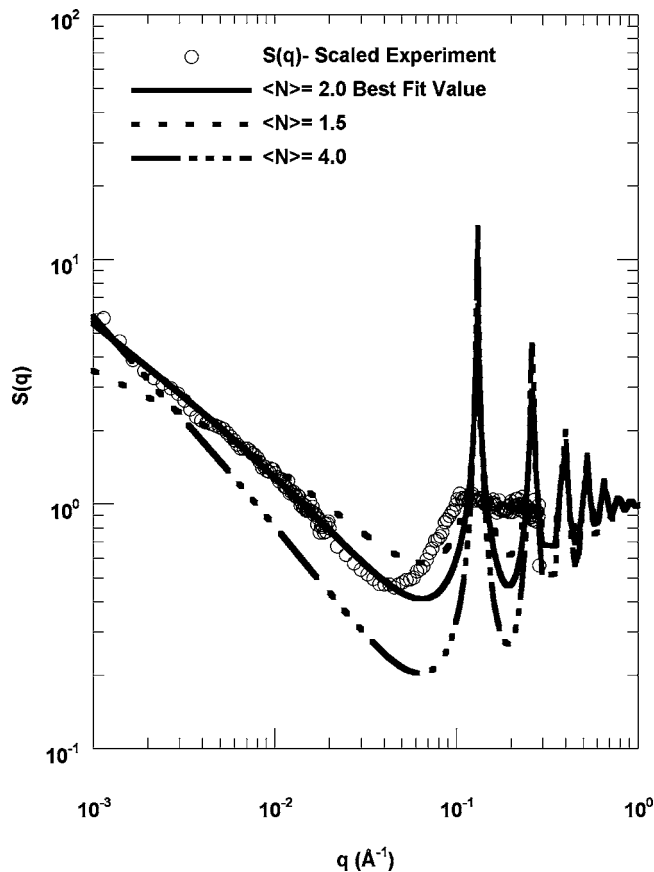
FIG. 5. The scaled experiment data for $S(q)$, circles, are obtained by taking the ratio of the experimental intensity to that of the calculated single-plate scattering for 0.008 volume fraction Cloisite 6A in p-xylene-d10. The amplitude and background corrections from Table II were applied to the calculated values. We compare this with $S(q)$ calculated from the model distribution with $y=1$. Here, k parameters corresponding to three different average numbers of layers per stack ($\langle N \rangle$) are displayed. The best-fit value from Table II provides an excellent description of the low-q dependence. At higher q, our data exhibit an elevated background due to incoherent scattering and the form factor for neutron scattering is small hence we do not observe the peaks in $S(q)$. However, these are observed in SAXS, as detailed in Fig. 4.

H. SANS fits

We next explore the values for k and y for the layers-per-stack distribution in Eq. (14). In our first trials we freely varied both k and y over a wide range while comparing to the SANS data for a selected composition, 0.008 volume fraction. We determined that fits to the data all drive y towards unity. Therefore, we set $y=1$ and then used least-squares analysis to obtain best-fit values for the parameter k. From Eq. (14), we see that $y=1$ implies the distribution of layer spacings is a power law, n^{-k}. Evidently values of $k>2$ are required to obtain a finite mean number of layers in a stack.

To illustrate, an example is provided in Fig. 5. We calculate an experimental structure factor by dividing the scattering data by the single-sheet terms in Eq. (7). These points are then compared with $\langle S(q) \rangle_{P,\Omega}$ [Eq. (17)]. Note that the Dawson function factor (resulting from angular averaging) is included in Eq. (7). As the value of k is varied, the average number of sheets per stack $\langle N \rangle$ is changed. Comparison with the experimental structure factor shows that an excellent description of the low q dependence is obtained. At higher q, $\langle S(q) \rangle_{P,\Omega}$ exhibits a diffraction-like peak, absent in the data. This is expected. The SANS data are affected by both a small neutron form factor in this q range and a significant incoherent background, together they obscure any evidence of the peak in the experimental structure factor (see Fig. 6). The peak is, of course, observed in x-ray scattering, as described above.

I. Summary of SANS fits

Samples spanning a range in Cloisite 6A content from 0.005 to 20 wt. % were prepared in p-xylene-d10. As shown in Table II, these span a volume fraction of 4×10^{-5} to 0.16. One might expect that at the lowest concentrations, scattering from a single plate would be observed. However, it is evident in Fig. 6 that all concentrations show power law behaviors which are steeper than q^{-2}, which would be the signature of scattering from single plates (compare with Fig. 3).

The absolute scattered intensity clearly rises with clay content. We calculate the scattering invariant, $\int_{q_{\min}}^{q_{\max}} q^2 I(q) dq$,

TABLE II. Summary of fitting parameters. Common factors for all fits: $\xi=3$, $y=1$, and $R=32\,000$ Å. For p-xylene and CDCl$_3$ $\Delta=48$ Å. For TDF $\Delta=46$ Å. See text for details.

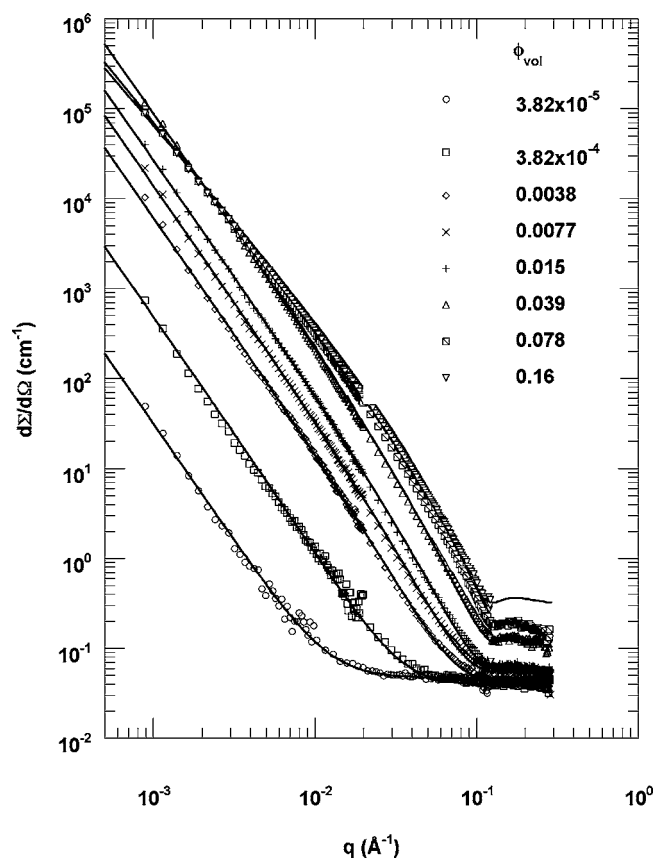| Sample	Wt. %	Volume Fraction	A	B cm^{-1}	k	$\langle N \rangle$
Xylene 005 wt.	0.005	3.824×10^{-05}	0.59	0.047	-2.529 ± 0.19	1.88 ± 0.45
Xylene 05 wt.	0.05	3.824×10^{-04}	0.92	0.040	-2.674 ± 0.14	1.64 ± 0.18
Xylene_pt 5 wt.	0.5	3.828×10^{-03}	1.16	0.044	-2.471 ± 0.05	2.02 ± 0.14
Xylene 1 wt.	1	7.665×10^{-03}	1.31	0.054	-2.467 ± 0.05	2.03 ± 0.14
Xylene 2 wt.	2	1.537×10^{-02}	1.27	0.060	-2.475 ± 0.04	2.01 ± 0.12
Xylene 5 wt.	5	3.869×10^{-02}	1.71	0.117	-2.495 ± 0.12	1.96 ± 0.28
Xylene 10 wt.	10	7.831×10^{-02}	1.30	0.161	-3.002 ± 0.12	1.37 ± 0.07
Xylene 20 wt.	20	1.605×10^{-01}	0.79	0.323	-3.291 ± 0.21	1.25 ± 0.07
TDF	2.58	2.061×10^{-02}	1.28	0.137	-2.784 ± 0.03	1.52 ± 0.03
CDCl$_3$	2.50	3.019×10^{-02}	0.73	0.052	-2.701 ± 0.07	1.61 ± 0.09

FIG. 6. The scattering data from Cloisite 6A in *p*-xylene-*d*10 are compared with lines calculated from the model parameters in Table II. Individual organoclay sheets assemble into structures that are laterally extended and vertically stacked. The distribution of stack heights are described by a probability distribution described in the text. To attain these fits we require amplitude factors, which are linear in clay volume fraction up to 5 wt. % clay, and incoherent backgrounds, which are linear in clay volume fraction throughout (see Table II).

where $q_{min} = 10^{-3}$ and $q_{max} = 0.29$ Å^{-1}, and find that this quantity is linear in clay volume fraction except for the very lowest concentrations. We may also simply normalize each scattering curve to the clay volume fraction. In that case we find that the scattering per unit clay volume at first rises, then it falls for concentrations above 5 wt. % (0.04 volume fraction). A possible origin of this effect is that there are additional inter-particle correlations at these higher clay contents.

We fit our data with Eq. (18). Along with the *k* parameter from our model distribution for polydisperse stacks, we allow the *A* and *B* to vary. We utilize a least-squares fitting procedure.

The resulting parameters are listed in Table II and the calculated lines from the fits are compared with the data in Fig. 6. As is evident from the figure, Eq. (18) provides an excellent description of the data. We estimate the uncertainty in *k* by examining the distribution of chi-square values about the best-fit value. From this, we select a 90% probability and report this as the estimated standard deviation (ESD) of the values in Table II. We also calculate the corresponding distribution for values of $\langle N \rangle$. The overall impression is that our fits are very well constrained.

J. Varying solubility parameter

To test for possible effects of changes in the solubility coefficients on the structures, we utilized two additional solvents (CDCl$_3$ and TDF) that exhibit an ability to disperse organoclay. As already discussed, among the three solvents TDF has the greatest polarity. The scattering from these two samples were examined with both SANS and USANS. The latter data allow us to further investigate the range of length scales applicable to this model.

The data sets for both CDCl$_3$ and TDF solvents exhibit intensity variations with q that are similar to the *p*-xylene data. Furthermore, the uniform power law extends to nearly the lowest q values accessible for USANS. We begin to see a rollover only at q values less than $\sim 5 \times 10^{-5}$ Å^{-1}. We expect to see deviations from the power law at wave numbers of order $1/R$, where *R* is the transverse dimension of the stack of layers. To account for the observed behavior a quite large value of *R* is required.

We have selected the smallest *R* value consistent with these data (32 000 Å), and held it fixed as the same three parameters as above—amplitude, incoherent background, and *k* parameter—were varied. The resulting fits capture very well the behavior over the wide range in scattered intensity and *q*. The *k* parameters are similar to those obtained from fits to the *p*-xylene data.

A clear implication from the USANS data is that the lateral dimension of the clay structure is quite large, much larger than any one organoclay sheet. The tactoids in our samples must therefore consist of overlapping clay sheets, and not simply stacks in which the individual sheets are arranged like a well-ordered pack of cards. Rather, the individual sheets must be arranged more like a pack of cards that has been scattered onto a tabletop. Such an arrangement would lend the necessary rigidity and flatness to the tactoid, such that it could scatter coherently across its transverse dimension, as assumed in the scattering model we have presented.

Such a large lateral dimension as we find from the US-ANS data suggests that extended structures of ~ 6 μm should be present in these samples. Consistent with this, such fluids are rather turbid in appearance, and through optical microscopy we do observe some particles in this size range. Given the population of stack heights (see distribution of *N* in Fig. 8), we would expect only a few particles to have sufficient thickness to be observable in optical microscopy.

III. DISCUSSION

The scattering data are well described by a model consisting of tactoids having a polydisperse number of layers. However, the distribution of this number is significantly constrained by the scattering data. We have already demonstrated this in Fig. 5. In Table II and Fig. 7 are summarized the results for fits to all of our data. For most of the data the average tactoid is about two sheets. Higher volume fraction *p*-xylene samples show a somewhat reduced size.

Examination of the distribution functions (Fig. 8) of the number of sheets per tactoid shows that the most probable number of sheets per tactoid is one (with about 80% prob-
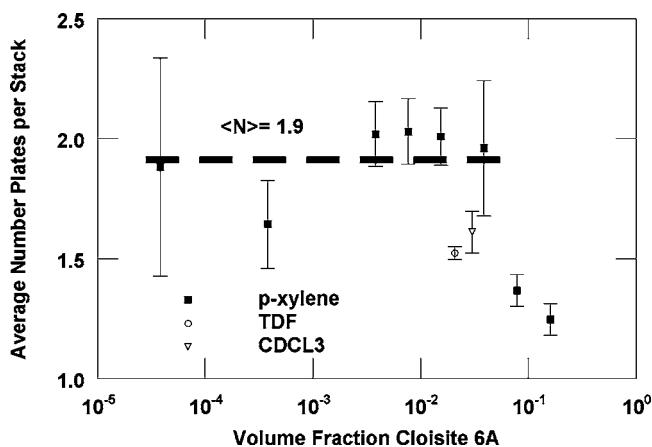
FIG. 7. The average tactoid sizes, as calculated from fitted parameters for distributions of the number of layers per stack, are essentially invariant across a very broad concentration range for *p*-xylene. The slightly lower values for TDF and CDCl₃ are only marginally outside the estimated error range. The highest concentration *p*-xylene samples exhibit significantly lower average stack heights, which may result from inter-tactoid correlations.

ability). The next most probable number is two (with about 10% probability), with the remaining percentage distributed over tactoids with larger number of sheets. Although the distribution is not bounded to any finite number, essentially all of the tactoids fall in the range $N \leq 10$.

Our description of polydisperse tactoids has so far neglected the distribution in lateral dimension of the tactoid. The USANS data indicates that the transverse dimension R of the tactoids is at least 32 000 Å. What is the possible range of R values? In Fig. 3, we display intensity profiles for several values of R. Note that small values of R produce an intensity profile that is essentially identical to that for larger R in the high q regime. However, at lower q the intensities from tactoids with smaller R values approach a q-independent limit, the value of which depends on R.

Evidently, the summation of intensities from any distribution of tactoids having significant numbers with small R val-
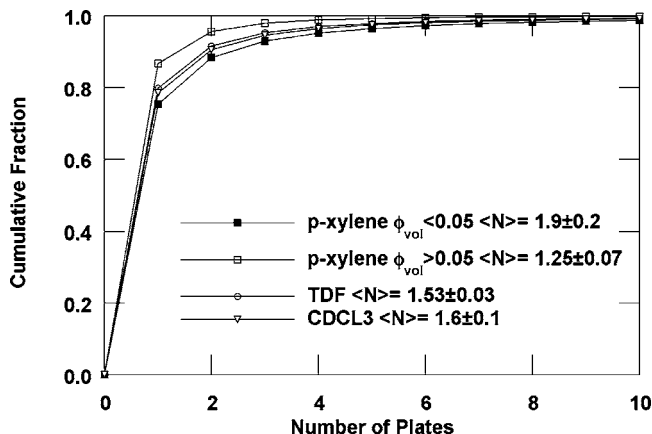

FIG. 8. Cumulative distributions for the number of sheets per tactoid calculated from data in Table II for four representative examples. Note that in each case the most probable number of sheets per tactoid is one. Also indicated is the average number of sheets for each example.
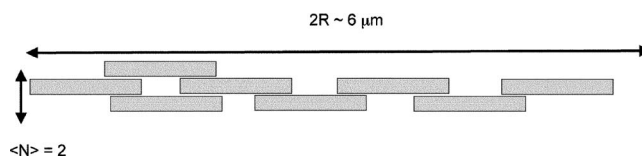

FIG. 9. Tactoid structure suggested by scattering parameters. Overall dimension set by extended power law to lowest q values from USANS. Our distribution for the number of layers per stack suggests the average number of sheets per stack is about 2, but the frequency of single sheets is nearly 80%.

ues will reduce the intensity at low q. Comparison of the calculated intensities for binary blends of large and small R tactoids with the experimental data demonstrates that only large R values are consistent with the data. A more precise description of the R values is not possible, and we select the largest R value as typical for all tactoids in the sample.

The resulting model for the tactoids is shown in Fig. 9. This structure, with its randomly overlapping clay sheets, satisfies the requirement that the transverse dimension R is much larger than that of an individual sheet. Polydispersity in the number of layers in a stack is also a natural outgrowth of this structure: in a tactoid made of overlapping sheets we see how about 80% of $N=1$ regions can be mixed with $N \geq 2$ regions. Evidently, the lowest-energy state for two overlapping sheets is that they be fully overlapping, i.e., in contact over their entire area. One might naively suppose that two sheets brought into partial overlap would be driven by steadily decreasing van der Waals energy to slide together, reaching full overlap. However, such a process might well be interrupted by various imperfections in the sheets, including random potentials resulting from the random locations of substitutional atoms in the clay crystalline matrix. Thus a state of partial overlap of two or more sheets might be metastable.

Tactoids such as these are consistent with gel formation at very low clay contents, as we will discuss in the next part of the paper.

IV. ORGANOCLAY RHEOLOGY

A. Experimental procedure

Samples were prepared similarly to those for the scattering experiments except here we used *p*-xylene-*h*10. Samples of about 25 ml volume were stirred for at least 24 h and stored in air-tight glass vials until use. The resulting dispersions had a somewhat turbid, brownish color. At the higher concentrations they displayed typical gel behavior such as trapping of air bubbles and lack of flow when the container is tipped. Over the several weeks duration of the experiments no evidence of phase separation was seen.

Portions of these dispersions were pipetted into a Couette-geometry cell (0.5 mm gap). The experiments were performed on a Rheometrics RFS II Rheometer, where we equipped the sample cell with a vapor trap to prevent *p*-xylene loss. Because it is well known that such gels can display significant history-dependent behavior, we performed the experiments in a fixed sequence.

We first determined the range of linear stress through a strain sweep up to about 10%. Following conventional practice, we then performed a frequency sweep always keeping the strain well below the non-linear limit. Having established that these data were satisfactory, we then applied steady shear to the sample, sweeping the strain rate from the lowest to highest values. As is apparent in this data, significant shear thinning is observed.

B. Modeling clay rheology

The mechanical shear properties of suspensions depend on many factors including the shape of the particles, the interactions between the particles, and the particle volume fraction, ϕ. Water-soluble Laponite clays are well known for forming space-filling elastic "gels" at dilute ϕ [16]. These clay suspensions have many characteristics of glassy solids and are known to age as the ionic strength of the water changes due to partial dissolution. The surface charges on the Laponite platelets have opposite signs on the faces and edges, so the structure of many platelets can resemble a house of cards.

By contrast, Cloisite organoclays dispersed in organic solvents are not expected to interact through spatially separated surface charges of opposite sign. Ideally, the organoclay platelets are completely dispersed and have hydrocarbon coatings that are not sticky; such organoclay dispersions would then resemble the more idealized case of "hard" platelets in solution. In reality, and in accordance with our scattering results, it appears that this idealization is not true for the real organoclays we have studied. Instead, tactoid structures consisting of several platelets are dispersed in solution. Since these tactoids themselves have very large aspect ratio, they resemble pseudoplatelets, and a model of jamming of randomly-oriented tactoids with attractive interactions could offer a consistent explanation of structural and rheological properties.

If clay tactoids did not interact through strong attractions compared to the thermal energy, then the rheology of the clay suspension would be expected to change dramatically when ϕ is raised above an effective overlap volume fraction, ϕ^*. It is well known that the onset of elasticity in polymer solutions is associated with an overlap concentration C^*, at which the coils effectively "touch." For polymer concentrations above C^*, neighboring polymer coils overlap and entangle, producing a suspension that has a dominant entanglement elasticity. An analogous argument borrows the essential idea behind the overlap concentration for polymer coils [35] and applies it to clay tactoids.

The high aspect ratio and platelike shape of the clay tactoids would enable them to effectively fill volume at relatively dilute ϕ. Suppose that the tactoids can be considered as thin microscale disks having radius R and thickness $h \ll R$ which are randomly oriented. Then, in terms of packing or jamming, each disk should be regarded as occupying a volume $V_{\mathrm{eff}} = 4\pi R^3/3$, which is of course much larger than its actual displaced volume V: $V_{\mathrm{eff}} = [R/(3h)]V$. Of course, this is an idealization, since real tactoids are not disklike in shape, but this assumption simplifies the model.

One can crudely estimate that the randomly oriented clay tactoids will "touch" and fill space at a volume fraction: $\phi^* \approx \phi_{\mathrm{MRJ}}(V/V_{\mathrm{eff}}) = \phi_{\mathrm{MRJ}}(3h/R)$, where $\phi_{\mathrm{MRJ}} \approx 0.64$ is the volume fraction associated with random close packing [36] or the "maximally random jammed" (MRJ) configuration of spheres. Thus, for $R=3$ μm and $h=100$ Å ($N=2$ and $\Delta =50$ Å), one finds $\phi^* \approx 0.006$, or only a few percent is needed to achieve overlap. At higher $\phi > \phi^*$, tactoids without attractive interactions would, for steric reasons, begin to form nematic phases having orientational order. Such nematic phases exhibit birefringence. Thus, performing a combination of optical birefringence measurements and rheology can be useful to unravel the structure-rheology relationship of organoclays.

In contrast, dispersions of strongly attractive particles can form percolating gels that have considerable elasticity due to the rigidity of the networks of solids. Fractal gels of solid spherical particulates at very dilute $\phi < 10^{-2}$ typically are weak and fragile, and gravitational forces generally cause such gels to collapse. However, at larger $\phi \approx 0.1$, the arms of the gel are comprised of densely packed particles. These particles have enough nearest neighbors to create a locally glassy disordered structure that can support significant shear stresses and inhibit gravitationally driven collapse. Optical microscopy is typically used in tandem with rheology to identify the percolating network structures that characterize this type of particulate gel material [37]. The structural hallmarks of attractive percolating gels are networks of densely packed static particles that reside in the bare solvent; spatial heterogeneity is observed.

The organoclay system used in this study has several characteristics that differ from the idealized picture of weakly interacting disks. The tactoids are not circular disklike platelets that are completely uniform in size and shape, but are instead rectangular platelets having varying aspect ratios and a considerable polydispersity in lateral dimensions. Also, the tactoid-tactoid interactions as a function of relative orientations and separation have not been characterized. Therefore, the model presented above can only be used as a crude guideline for estimating an effective overlap volume fraction for the organoclays used in the present study.

C. Cloisite rheology

For Cloisite organoclays in the aromatic solvent p-xylene, we have measured the linear shear viscoelasticity using small amplitude oscillatory rheometry, the yield stress through steady shear viscometry, and the optical birefringence using cross polarizers. We find that there is a strong increase in the plateau elastic modulus, G_{p}', and yield stress, τ_{y}, with respect to ϕ. Moreover, the onset of the dominantly elastic behavior occurs at only a few volume percent.

Frequency-dependent data (10^{-1} to 10^2 rad s^{-1}) for the storage and loss moduli, $G'(\omega)$ and $G''(\omega)$, respectively, exhibit typical solidlike behavior for volume fractions over nearly the entire range of compositions. There is a dominant elastic plateau modulus that is relatively independent of frequency. This is accompanied by a frequency-independent loss modulus, approximately an order of magnitude smaller.
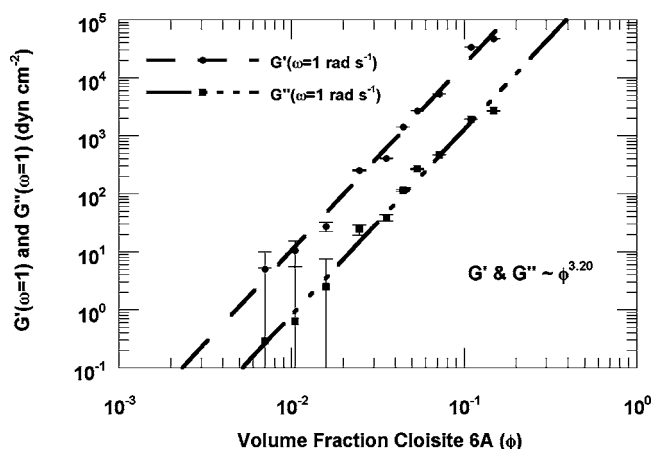
FIG. 10. Storage (G') and Loss (G'') moduli exhibit power law scaling versus volume fraction organoclay. The expected scaling of ($\phi - \phi^*$) where ϕ^* is the overlap concentration is not observed because ϕ^* is small.

At our lowest clay contents, $\phi = 0.007$, the torques are just at the limit that can be measured; giving the low frequency data large error bars. Consequently, at this ϕ, it is not clear whether the rheology is dominantly elastic or viscous; the two contributions are comparable within our ability to measure them.

The volume fraction dependence of the storage modulus and loss modulus taken at $\omega = 1$ rad s are shown in Fig. 10. Over the entire volume fraction range probed, the storage and loss moduli increase as $G'_p(\phi) \sim \phi^{3.2}$, and G'' remains about an order of magnitude lower than G'. One might have expected a scaling with respect to ($\phi - \phi^*$), but we can safely ignore ϕ^* because the overlap concentration is small. This rapid power law increase in the elastic modulus is indicative of the increasingly strong jamming of the clay platelets and, possibly, nematically oriented domains of clay platelets.

As we previously discussed, Mourchid *et al.* [15,19] obtain a power law for $G'_p(\phi) \sim \phi^{\alpha}$ of $\alpha = 2.3$ for Laponite gels. Trappe and Weitz [37] find a power law $-\alpha = 4.1$ for a gel of weakly attractive particles. They characterize such a value as typical for elasticity percolation in three dimensions in which a few strong bonds significantly increase the modulus. A comparison of our measured value of $\alpha = 3.2$ with these values suggests, as we previously speculated, that the interparticle interaction for the organoclays is weak. At the very lowest ϕ, the error bars for the storage and loss moduli overlap, and we would eventually expect a dominant loss modulus as the volume fraction is further decreased toward the pure p-xylene limit.

Steady shear measurements of soft elastic materials can be affected by shear banding [38] in which a narrow band of the material becomes less viscous due to a local change in the particle concentration. This shear banding can lead to a spatially inhomogeneous shear rate in the material filling the gap between the solid surfaces of the rheometer. In such cases, the viscosity that the rheometer reports is an "effective viscosity" since the true velocity field in the gap cannot be directly measured. As a precaution, we vary the shear rate from low to high in order to avoid hysteresis in the rheology
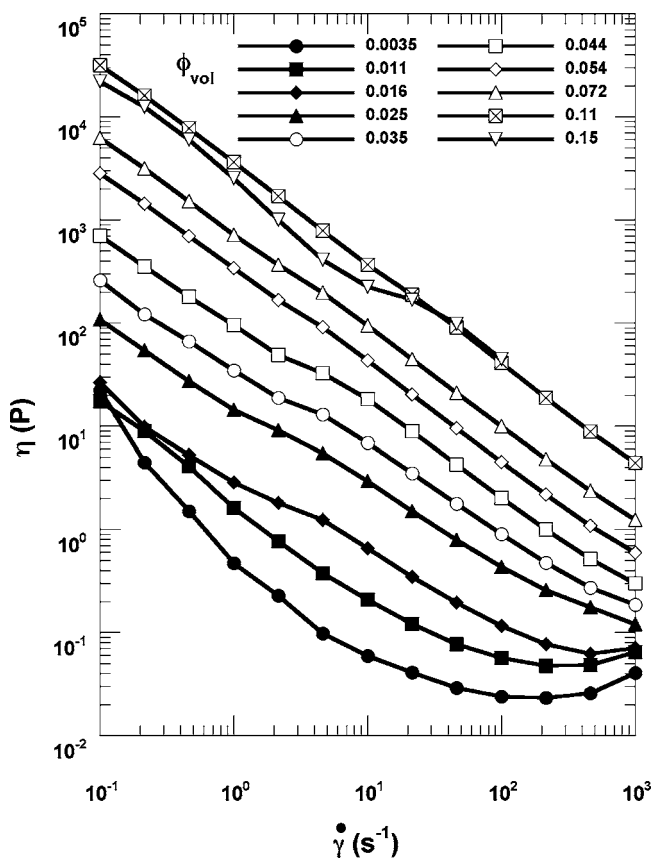

FIG. 11. Steady shear viscosity for indicated volume fractions of Cloisite 6A in p-xylene. Shear thinning is evident across the entire composition range. We vary the shear rate from low to high in order to avoid hysteresis in the rheology.

that might be caused by subjecting the system to high shear rates.

We find that the effective viscosity as a function of shear rate for the organoclays, shown in Fig. 11, is highly shear thinning, with nearly all of the curves reflecting $\eta(\dot{\gamma}) = \tau_y / \dot{\gamma}$ toward lower shear rates. This strong shear thinning is characteristic of soft elastic solids that yield when the applied shear stress exceeds τ_y. At the highest shear rates and lowest ϕ, we find that the viscosity tends toward the limit of the pure p-xylene, which has a viscosity, $\eta_0 \approx 1$ cP.

In Fig. 12, we plot $\tau_y(\phi)$, which also exhibits a very strong rise with volume fraction: $\tau_y \sim \phi^3$. As we discussed above, a similar scaling was observed for Laponite gels [16]. Those authors report corresponding small angle light scattering data having a power law slope for the intensity versus q of -1.8, but no such scattering signature accompanies our results. It is possible that the larger aspect ratio for the organoclay pushes this power-law regime outside our experimental window.

Within measurement error, the observed power law for the yield stress $\tau_y(\phi)$ is identical to the dependence we have found for G'_p. This is not surprising, since the yield stress is known to follow the storage modulus and is typically about an order of magnitude lower than G'_p for many soft materials, including emulsions. From this measurement, we can identify the yield strain, $\gamma_y = \tau_y / G'_p$, as being $\gamma_y \approx 0.1$ for the or-
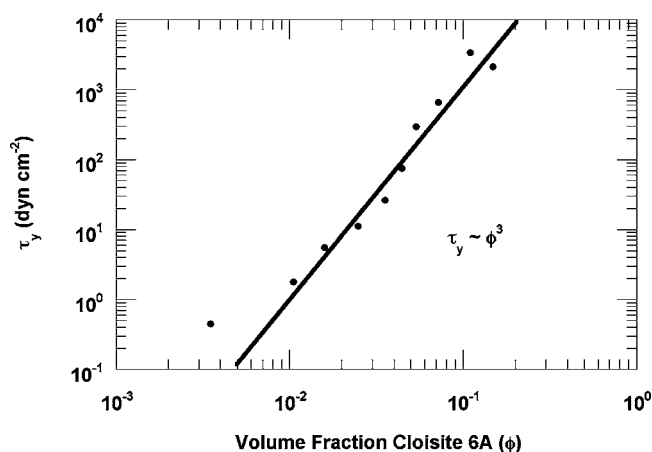
FIG. 12. Yield stress τ_y, defined as $\tau_y = \eta(\dot{\gamma})\dot{\gamma}$ for $\dot{\gamma} \to 0$, shows a power law scaling with volume fraction clay equal, to within error, to that for the storage modulus, $G' \sim \phi^{3.2}$. A similar scaling of yield stress has been observed for Laponite gels (see text).

ganoclays, consistent with determinations of the linear response regime for oscillatory stress.

Overall the rise in the plateau modulus and yield stress of the organoclays begins at very dilute concentrations; from this, we can roughly identify $\phi^* \approx 0.01$, consistent with the simplistic model. Thus, for dispersions of clay platelets, this rise in the elasticity occurs at much lower ϕ than for hard spheres, for which it is observed at the colloidal glass transition, around $\phi_g = 0.58$ [39].

In the case of colloidal hard spheres, the magnitude of the plateau modulus near the glass transition is set by the thermal energy divided by the available translational free volume per particle: $G'_p \sim k_B T/V_f$. Here, in the case of platelets, we invoke the previous estimate of the effective jamming volume fraction of randomly oriented tactoids, to assert that the volume fraction associated with the glass transition would be around the estimated overlap concentration ϕ^*. Such randomly oriented hard clay tactoids would form a disordered glass at volume fractions at below one volume percent, as we have observed. Weak attractive interactions in the organoclay system would reduce this volume fraction associated with the onset of elasticity somewhat.

Birefringence measurements of the organoclay solutions indicate that there are nematically ordered domains of the organoclay tactoids for $\phi \gtrsim 0.01$. Therefore, domain boundaries between different nematic regions are likely to influence our rheological measurements, and any theoretical models of the rheology of organoclays would need to include this effect. Obviously, the simplistic model we have presented of a disordered glass of randomly oriented tactoids needs to be modified to include nematic domains as the volume fraction is increased above the effective jamming transition around ϕ^*.

V. CONCLUSIONS

We have shown that a structural model for dispersions of organoclay sheets in organic liquids can be constructed starting from the basic building block for an organoclay, a sur-

factant covered metal oxide sheet. This model can account for the x-ray and neutron scattering over a very wide q range, indicating that the model captures structural details over many length scales—from near-neighbor intersheet correlations to multisheet, several-micrometer sized agglomerates. It is important to recognize that there are various ways to obtain a power law of q^{-3} – surface fractal, power-law distribution of spheres, power-law distribution of number of layers. Our success in building a well constrained model was through the use of SAXS and rheology data, which provided additional information regarding the geometry of possible structures.

For the individual sheets, neutron SLD measurements show that surfactants are liberated from the surface. Recognizing that there is significant experimental uncertainty, these data nevertheless suggest that organoclay evolves to an equilibrium surfactant content that achieves charge balance for each sheet. To our knowledge, this is the first *in situ* measurement of this effect.

Our structural model describes the way in which these surfactant-coated sheets associate with one another in a solvent. Several lines of reasoning suggest that, for our samples, a multisheet stacking is present; for example, inter-lamellar correlation peaks are observed in x-ray scattering. However, the rheology clearly indicates a gel state, inconsistent with merely a low-concentration suspension of multi-sheet tactoids. Also the neutron scattering is clearly inconsistent with either dispersed single sheets or with a suspension of macroscopic particles (i.e., Porod scattering). A mixture of partly disassociated sheets is clearly suggested, and our model consists of two sorts of associations.

First, we construct a function to describe the distribution of the number of sheets per stack in our samples. Fitting this function to our scattering data reveals that the most probable number of sheets per stack is one. This is for samples that span a variety of concentrations, as well as three solvents with different polarities. Some variation in the distributions are observed resulting in the average number of sheets per stack varying from about $\langle N \rangle = 2$ to $\langle N \rangle = 1.25$.

On the basis of previous work, one might have expected more variation among the different samples. For example, clay dispersions in $CDCl_3$, which previous authors [22] had suggested consisted of only individual dispersed sheets, is shown here to contain several percent of multisheet stacks. The inclusion of a wider q range for our neutron scattering data helps resolve the small, but significant number of multisheet stacks.

The second multisheet association we find is in the lateral direction. The USANS data indicates that the transverse dimension R of the tactoids is at least 32 000 Å; moreover, the overall scattered intensity indicates that essentially all sheets are components of these large aggregates. Combined with multistack associations, the resulting model for the tactoids is a plate-like structure with randomly overlapping clay sheets (Fig. 9).

A signature of the proposed structure is a dependence of the scattering intensities on wave number q that follows a power law of the form $I \sim q^{-x}$, where $x \sim 3$. The wide q range for this power-law behavior is a direct consequence of the large lateral dimension of the aggregate. This unusual power-

law form has been seen in several studies of clay suspensions. For example, Pignon *et al.* [16] observe this behavior for $1.2 \times 10^{-4} < q < 3 \times 10^{-3}$ Å^{-1} for Laponite suspensions in water. From the rolloff at low q in the data of Ref. [16], we can estimate the lateral dimension for the tactoids there as $R \sim 13\,000$ Å, comparable to the $R \sim 32\,000$ Å value we find. This smaller dimension for Laponite is consistent with the smaller lateral dimension of each disk (30 nm) compared to those for Cloisite (~ 150 nm).

The large aggregate size is consistent with the rheology, which shows that gel formation occurs at extraordinary low volume fraction. What is less well understood is the power-law scaling of the storage modulus, loss modulus and yield strength with clay volume fraction. All scale approximately with ϕ^3. Previous studies of weakly associating media had suggested that a power law scaling of ϕ^4 should be expected for suspensions of interacting materials. Our data seemingly indicate that the interactions here are weak, but this seems to contradict the structural observation that each sheet is bound into an aggregate. The observation of yield strength scaling with Laponite volume fraction to a power of three has been previously reported by Pignon *et al.* [16]. However, those authors also reported the appearance of a structure having fractal dimension of 1.8, evidenced by light scattering data. Such a signature is not found here.

ACKNOWLEDGMENTS

APPENDIX A

We assume the sheets individually to be disks of radius R with a cross-sectional density profile $f(z)$. The displacement along the z axis between the centers of adjacent sheets is taken to be Δ on average, plus random noise as described below. The density in real space of such an assemblage is then

$$\rho(r_\perp, z) = g(r_\perp) \int dz' \sum_{k=1}^{n} \delta(z - (z' + k\Delta + \zeta_k)) f(z') \tag{A1}$$

in which ζ_k is the random part of the z coordinate of the kth layer, and $g(r_\perp) = \theta(R - |r_\perp|)$ describes a disk profile in the transverse direction. We assume the variations in spacing between the kth and $k+1$st layers, denoted ξ_k, to be independent Gaussian random variables with zero mean and variance ξ^2.

The structure factor $S(q)$ is given by

$$S(\vec{q}) = \langle \rho(\vec{q}) \rho(-\vec{q}) \rangle, \tag{A2}$$

where the angle brackets denote the average over the random spacing variables. To compute this average, we first compute the Fourier transform of the density profile $\rho(r)$ given above. The result is

$$\rho(q_\perp, q_z) = \widetilde{g}(q_\perp) \widetilde{f}(q_z) \sum_{k=1}^{n} e^{iq_z k\Delta + iq_z \zeta_k}. \tag{A3}$$

The product $\rho(q)\rho(-q)$ is then

$$\rho(q)\rho(-q) = |\widetilde{g}(q_\perp)|^2 |\widetilde{f}(q_z)|^2 \sum_{k=1}^{n} \sum_{k'=1}^{n} e^{iq_z \Delta(k-k')} e^{iq_z(\zeta_k - \zeta_{k'})}. \tag{A4}$$

The difference $\zeta_k - \zeta_{k'}$ is a sum of $|k - k'|$ of the Gaussian random variables $\{\xi_j\}$, each with zero mean and variance ξ^2. This sum itself is a Gaussian random variable, of zero mean and variance $|k - k'| \xi^2$. We perform the average over this random variable to obtain

$$\langle \rho(q)\rho(-q) \rangle = |\widetilde{g}(q_\perp)|^2 |\widetilde{f}(q_z)|^2 \sum_{k=1}^{n} \sum_{k'=1}^{n} e^{iq_z \Delta(k-k')} e^{-(1/2)q_z^2 \xi^2 |k-k'|}. \tag{A5}$$

The double summation can be performed explicitly, as follows. For notational convenience we define $x = \exp[-(1/2)q_z^2 \xi^2]$ and $\beta = q_z \Delta$. The desired double sum $\Sigma_\nu(\xi, \beta)$ is

$$\Sigma_n(x, \beta) = \sum_{k=1}^{n} \sum_{k'=1}^{n} x^{|k-k'|} e^{i\beta(k-k')}. \tag{A6}$$

Separating the terms with $k = k'$ from the rest, and grouping terms with indices $\{k, k'\}$ together with $\{k', k\}$, we have

$$\Sigma_n(X) = n + 2\,\text{Re}\left[\sum_{k'=1}^{n} \sum_{k=k'+1}^{n} X^{k-k'} \right] \tag{A7}$$

in which we have defined $X = x \exp(i\beta)$. Now our sums are in the form of geometric series, and can be given in closed form. After a bit of arithmetic we find

$$\Sigma_n(X) = n + 2\,\text{Re}\left[\frac{X^{n+1} + nX(1 - X) - X}{(1 - X)^2} \right], \tag{A8}$$

which is the Kratky-Porod result. We then have for the structure factor of a stack of n sheets, each a disk of radius R with density profile $f(z)$, the result

$$S(q_\perp, q_z) = |\widetilde{g}(q_\perp)|^2 |\widetilde{f}(q_z)|^2 \Sigma_n \{\exp[iq_z \Delta - (1/2)q_z^2 \xi^2]\}. \tag{A9}$$

Now we consider the angular average of this structure factor over the orientation of the stack. Our discussion here parallels that of Richter *et al.* [27]. Equivalently we may average over the direction of the wave vector q. This leads to

$$\langle S(q) \rangle_\Omega = \int_0^1 d\mu S(q\sqrt{1-\mu^2}, q\mu). \qquad (A10)$$

where $\mu = \cos(\theta)$ the cosine of the angle between the wave vector q and the sheet normal.

In evaluating this angular average, we make use of the fact that the stack of sheets has a large aspect ratio. Suppose that the wave number q is probing the structure of the stack, i.e., that q times the total stack thickness H is of order unity. The stack has a large aspect ratio, so $H/R \ll 1$. Hence qR is very large. We expect that $g(q_\perp)$ becomes very small when $q_\perp R$ becomes large. This restricts the angle between the wave vector and sheet normal to be very small, as we now show.

Recalling that $g(r_\perp)$ is the transverse profile of a disk of radius R, then $g(q_\perp)$ becomes the form factor

$$\tilde{g}(q_\perp) = \frac{2\pi R^2 J_1(q_\perp R)}{q_\perp R}, \qquad (A11)$$

which we further approximate with a Gaussian according to

$$(J_1(x)/x)^2 \approx (1/4)\exp(-x^2/4). \qquad (A12)$$

Expanding for small angles θ, we have $q_\perp R \approx qR\theta$. Thus we find that the angle θ between q and the layer normal is restricted to be less than of order $1/(qR)$.

Physically, we may say that only stacks nearly aligned with the wave vector contribute significantly to the scattering, because if a stack is tilted only a small angle away from perfect alignment, opposite ends of the stack will contribute out of phase with each other and thus interfere destructively.

With the angle so tightly restricted, q_z is nearly equal to q, and all the factors depending only on q_z in the structure factor come outside the angular integral. Using the disk form factor Eq. (A11) approximated as in Eq. (A12), we obtain

$$\langle S(q) \rangle_\Omega = |\tilde{f}(q)|^2 \Sigma_n \{\exp[iq\Delta - (1/2)q^2\xi^2]\} \frac{(\pi R^2)^2 D(qR/2)}{(qR/2)} \qquad (A13)$$

in which $D(u)$ is the Dawson function, defined by

$$D(u) = \exp(-u^2) \int_0^u dt \, \exp(t^2). \qquad (A14)$$

If our original assumption that qH is of order unity is not satisfied, but rather $qH \ll 1$ is valid, then we are in the "thin limit," in which the wave vector is no longer probing the stack structure. Then we can take the limit q_z approaching zero in $S(q)$ before angularly averaging. Again only the transverse form factor is affected by the angular average, whereupon we reach Eq. (A14) again, this time without requiring that qR be large.

Here we make use of well-controlled approximations in computing the angular averages, but it is also possible to compute the structure factor Eqs. (A10) or (A13) using direct numerical methods. This is the approach of Ho *et al.* [22], and we have numerically computed the structure factor using

values typical of that study: core thickness $2h = 10$ Å, inter-sheet spacing $\Delta = 50$ Å, sheet radius $R = 3000$ Å, standard deviation of sheet spacing $\xi = 3$ Å, and number of layers $N = 20$. We find the structure factor so computed has strong oscillations in the wave number range 0.003 Å$^{-1} < q < 0.1$ Å^{-1}, not observed in the data.

APPENDIX B

First we consider the scattering at small wave number resulting from a system of polydisperse spheres. The form factor for a sphere of radius R is

$$f_R(q) = 4\pi R^3 \frac{\sin(qR) - qR \cos(qR)}{(qR)^3}. \qquad (B1)$$

To compute the structure factor for a sample of randomly located polydisperse spheres, we average the square of this form factor over an assumed probability distribution for R. Here we take a power law distribution of R, and so obtain

$$S(q) \propto \int_0^\infty dR R^{-k} f_R(q)^2. \qquad (B2)$$

Substituting the explicit expression for the form factor, we have

$$S(q) \propto q^{-(7-k)} \int_q^\infty dx x^{-k} [\sin(x) - x\cos(x)]^2. \qquad (B3)$$

This integral converges for large x if $k > 3$ [for large x, we have approximately the integral of $x^{2-k}\cos^2(x)$]. For small x, we expand $\sin(x) - x < \cos(x) \approx x^3/3$, and see that for $k < 7$ the integral converges even as q approaches zero. Thus for $3 < k < 7$, we find for polydisperse spheres with $P(R)$ scaling as R^{-k}, the structure factor scales as $q^{-(7-k)}$.

APPENDIX C

Here we examine the behavior at smallish wave numbers of our scattering model, described in Sec. II F and Appendix A. By "smallish" we mean $q\xi \ll 1$, but not necessarily $q\Delta \ll 1$. Furthermore, we are interested in the limit $qR \gg 1$, i.e., very large transverse tactoid dimensions.

Thus we consider the large-argument limit of the Dawson function factor in Eq. (A13), $D(qR/2)/(qR/2)$. For large u, $D(u)/u$ scales as $1/u^2$; thus the factor $D(qR/2)/(qR/2)$ contributes a factor of q^{-2} to the q dependence of the structure factor [at all but the smallest wave numbers, where finite R leads to a rolloff in $S(q)$].

For $q\xi \ll 1$, the exponential factor resulting from randomness in intersheet spacing in Eq. (A5) may be dropped. Then the double sum becomes simply

$$\sum_{k=1}^N \sum_{k'=1}^N x^{k-k'} \qquad (C1)$$

which is actually a product of two arithmetic sums. After a bit of arithmetic, this sum can be shown to be

$$\Sigma_n\big|_{q_z\xi\to0} = \left(\frac{\sin(\Delta q_z n/2)}{\sin(\Delta q_z/2)}\right)^2 \tag{C2}$$

in which we have replaced x using its definition $x = \exp(iq_z\Delta)$.

As in Appendix A, the average over the tactoid orientation results in Eq. (A13), but with the above expression for Σ_n.

Now the average over the distribution of the number of layers in the stack, described in Sec. II F and leading to Eq. (17), can be simplified. We take the average of the limiting form of Σ_n over the pure power law limit of our layer distribution function $P_{k,y}(n)$ [i.e., $P_{k,1}(n) \sim n^{-k}$] to obtain

$$\langle\Sigma_n\big|_{q_n\xi\to0}\rangle_P \propto \sum_{n=1}^{\infty} n^{-k}\left(\frac{\sin(\Delta qn/2)}{\sin(\Delta q/2)}\right)^2. \tag{C3}$$

Now we go ahead and assume $q\Delta \ll 1$, but not $qn\Delta \ll 1$. After a bit of rearranging we have

$$\langle\Sigma_n\big|_{q\xi\to0}\rangle_P \sim q^{k-3}\sum_{n=1}^{\infty} n^{-k}\sin^2(\Delta qn/2). \tag{C4}$$

Because $q\Delta$ assumed small, the contributions from large n to the sum can be approximated by an integral, leading to

$$\langle\Sigma_n\big|_{q\xi\to0}\rangle_P \sim q^{k-3}\int_q^{\infty} dx\, x^{-k}\sin^2(x/2). \tag{C5}$$

This integral is convergent when q approaches zero for $k < 3$, and converges for large x when $k > 1$.

Hence for $1 < k < 3$ we find a power law for small wave number (but $qR \gg 1$) of q^{k-3}. Combined with the q^{-2} from the Dawson function factor, we have that $S(q)$ for small q scales as q^{k-5}. For values of k near $k = 2$, then, we have power laws around q^{-3}, consistent with the observed scattering data.

---

[1] T. R. Jones, Clay Miner. **18**, 399 (1983).

[2] C. A. Cody and W. W. Reichert, NLGI Spokesman **49**, 437 (1986).

[3] *Polymer-Clay Nanocomposites*, edited by T. J. Pinnavaia and G. W. Beall (John Wiley and Sons, Ltd., New York, 2000).

[4] *Crystal Structures of Clay Minerals and Their X-Ray Identification*, edited by G. W. Brindley and G. Brown (Mineralogical Society, London, 1984), Vol. 5.

[5] H. J. M. Hanley, C. D. Muzny, and B. D. Butler, Langmuir **13**, 5276 (1997).

[6] A. Weiss, Clays Clay Miner. **10**, 191 (1963).

[7] E. B. Sirota, D. M. Singer, and H. E. King, Jr., J. Chem. Phys. **100**, 1542 (1994).

[8] G. Lagaly and A. Weiss, in *Proceedings of the International Clay Conference*, Tokyo, 1969; G. Lagaly and A. Weiss, *Proceedings of the Reunion Hispano-Belga Minerales de la Arcilla*, Madrid, 1970; G. Lagaly, Clays Clay Miner. **30**, 215 (1982); G. Lagaly, Naturwiss. **68**, 82 (1981).

[9] R. A. Vaia, W. Liu, and H. Koerner, J. Polym. Sci., Part B: Polym. Phys. **41**, 3214 (2003).

[10] J. D. F. Ramsay and P. Linder, J. Chem. Soc., Faraday Trans. **89**, 4207 (1993).

[11] M. Morvan, D. Espinat, J. Lambard, and T. Zemb, Colloids Surf., A **82**, 193 (1994).

[12] M. Kroon, W. L. Vos, and G. H. Wegdam, Phys. Rev. E **57**, 1962 (1998).

[13] C. Shang and J. A. Rice, Phys. Rev. E **64**, 021401 (2001).

[14] J. N. Israelachvili, *Intermolecular and Surface Forces*, 2nd edition (Academic Press, New York, 1992).

[15] A. Mourchid, A. Delville, J. Lambard, E. Lécolier, and P. Levitz, Langmuir **11**, 1942 (1995).

[16] F. Pignon, A. Magnin, J.-M. Piau, B. Cabane, P. Lindner, and O. Diat, Phys. Rev. E **56**, 3281 (1997).

[17] J. M. Saunders, J. W. Goodwin, R. M. Richardson, and B. Vincent, J. Phys. Chem. B **103**, 9211 (1999).

[18] J. D. F. Ramsay, S. W. Swanton, and J. Bunce, J. Chem. Soc., Faraday Trans. **86**, 3919 (1990).

[19] A. Mourchid, E. Lécolier, H. Van Damme, and P. Levitz, Langmuir **14**, 4718 (1998).

[20] J.-M. Piau, M. Dorget, and J.-F. Palierne, J. Rheol. **43**, 305 (1999).

[21] B. K. G. Theng, *The Chemistry of Clay-Organic Reactions* (John Wiley and Sons, New York, 1974).

[22] D. L. Ho, R. M. Briber, and C. J. Glinka, Chem. Mater. **13**, 1923 (2001).

[23] S. J. Kemnetz, A. L. Still, C. A. Cody, and R. Schwindt, FATIPEC Congress Vol. II(19th), 17 (1988).

[24] D. L. Ho and C. J. Glinka, Chem. Mater. **15**, 1309 (2003).

[25] M. Yoonessi, H. Toghiani, T. L. Daulton, J.-S. Lin, and C. U. Pittman, Jr., Macromolecules **38**, 818 (2005).

[26] H. J. M. Hanley, C. D. Muzny, D. L. Ho, and C. J. Glinka, Langmuir **19**, 5575 (2003).

[27] D. Richter, D. Schneiders, M. Monkenbusch, L. Willner, L. J. Fetters, J. S. Huang, M. Lin, K. Mortensen, and B. Farago, Macromolecules **30**, 1053 (1997).

[28] M. A. Osman, M. Ernst, B. H. Meier, and U. W. Suter, J. Phys. Chem. B **106**, 653 (2002).

[29] I. A. Wiehe, Ind. Eng. Chem. Res. **34**, 661 (1995).

[30] C. J. Glinka, J. G. Barker, B. Hammouda, S. Krueger, J. J. Moyer, and W. J. Orts, J. Appl. Crystallogr. **31**(3), 430 (1998); NIST, *Cold Neutron Research Facility at the NIST, NG3 and NG7 30-Meter SANS Instruments Data Acqisition Manual* (National Institute of Standards and Technology, Gauthersburg, MD, 1999).

[31] J. G. Barker and J. S. Pedersen, J. Appl. Crystallogr. **28**, 105 (1995).

[32] J. G. Barker, C. J. Glinka, J. J. Moyer, M. H. Kim, A. R. Drews, and M. Agamalian, J. Appl. Crystallogr. **38**, 1004 (2005).

[33] M. A. Singh, S. S. Ghosh, and R. F. Shannon, Jr., J. Appl. Crystallogr. **26**, 787 (1993).

[34] R.-J. Roe, *Methods of X-Ray and Neutron Scattering in Polymer Science* (Oxford University Press, Oxford, 2000).

[35] P.-G. de Gennes, *Scaling Concepts in Polymer Physics* (Cor-

nell University Press, Ithaca, NY, 1979).

[36] P. Dimon, S. K. Sinha, D. A. Weitz, C. R. Safinya, G. S. Smith, W. A. Varady, and H. M. Lindsay, Phys. Rev. Lett. **57**, 595 (1986).

[37] V. Trappe and D. A. Weitz, Phys. Rev. Lett. **85**, 449

(2000).

[38] S. M. Fielding and P. D. Olmsted, Eur. Phys. J. E **11**, 65 (2003).

[39] T. G. Mason and D. A. Weitz, Phys. Rev. Lett. **75**, 2770 (1995).